Development and Evaluation of the Aerosol Forecast Member in NCEP's Global Ensemble Forecast System (GEFS-Aerosols v1)

Li Zhang[1,2], Raffaele Montuoro[1,2], Stuart A. McKeen[1,3], Barry Baker[4,5], Partha S. Bhattacharjee[6], Georg A. Grell[2], Judy Henderson[2], Li Pan[6], Gregory J. Frost[3], Jeff McQueen[7], Rick Saylor[8], Haiqin Li[1,2], Ravan Ahmadov[1,2], Jun Wang[7], Ivanka Stajner[7], Shobha Kondragunta[9], Xiaoyang Zhang[10], Fangjun Li[10]

[1]CIRES, University of Colorado, Boulder, CO, US;
[2]Global Systems Laboratory, Earth System Research Laboratory, NOAA, Boulder, CO, US;
[3]Chemical Sciences Laboratory, Earth System Research Laboratory, NOAA, Boulder, CO, US;
[4]NOAA Air Resources Laboratory, College Park, MD, US;
[5]Cooperative Institute for Climate and Satellites, University of Maryland, College Park, MD, US;
[6]I.M. Systems Group at NCEP/NWS/EMC, College Park, MD, US;
[7]Environmental Modeling Center, National Weather Service, Greenbelt, MD, US;
[8]NOAA Air Resources Laboratory, Oak Ridge, TN, US;
[9]NOAA/NESDIS Center for Satellite Applications and Research, Greenbelt, MD, US;
[10]Department of Geography, South Dakota State University, Brookings, SD, US

Submit to Geoscientific Model Development

March 2022

*Correspondence to: Li Zhang (kate.zhang@noaa.gov)
CIRES, University of Colorado Boulder
GSL EPAD, NOAA ESRL
325 Broadway David Skaggs Research Center R/GSL1
Boulder, CO 80305
1-303-497-3956

Abstract.

NOAA's National Weather Service (NWS) is on its way to deploy various operational prediction applications using the Unified Forecast System (https://ufscommunity.org/), a community-based coupled, comprehensive Earth modeling system. An aerosol model component developed in a collaboration between the Global Systems Laboratory, Chemical Science Laboratory, the Air Resources Laboratory, and Environmental Modeling Center (GSL, CSL, ARL, EMC) was coupled online with the FV3 Global Forecast System (FV3GFS) using the National Unified Operational Prediction Capability (NUOPC)-based NOAA Environmental Modeling System (NEMS) software framework. This aerosol prediction system replaced the NEMS GFS Aerosol Component (NGAC) system in the National Center for Environment Prediction (NCEP) production suite in September 2020 as one of the ensemble members of the Global Ensemble Forecast System (GEFS), dubbed GEFS-Aerosols v1. The aerosol component of atmospheric composition in GEFS is based on the Weather Research and Forecasting model (WRF-Chem). GEFS-Aerosols includes bulk modules from the Goddard Chemistry Aerosol Radiation and Transport model (GOCART). Additionally, the biomass burning plume rise module from High-Resolution Rapid Refresh (HRRR)-Smoke based on WRF-Chem was implemented; the GOCART dust scheme was replaced by the FENGSHA dust scheme (developed by ARL); the Blended Global Biomass Burning Emissions Product (GBBEPx version 3) provides biomass burning emission and Fire Radiative Power (FRP) data; and the global anthropogenic emission inventories are derived from the Community Emissions Data System (CEDS). All sub-grid scale transport and deposition is handled inside the atmospheric physics routines, which required consistent implementation of positive definite tracer transport and wet scavenging in the physics parameterizations used by NCEP's operational Global Forecast System based on FV3 (FV3GFS). This paper describes the details of GEFS-Aerosols model development and evaluation of real-time and retrospective runs using different observations from in situ measurement, satellite and aircraft data. GEFS-Aerosols predictions demonstrate substantial improvements for both composition and variability of aerosol distributions over those from the former operational NGAC system with the fundamental updates in atmospheric and chemical transport model.

1. Introduction

The operational air quality predictions in National Oceanic and Atmospheric Administration (NOAA)'s National Weather Service (NWS) contribute to the protection of lives and health in the US (https://airquality.weather.gov). These predictions are used by state and local air quality forecasters to issue official air quality forecasts for their respective areas. The U.S. Environmental Protection Agency (EPA) and the Centers for Disease Control and Prevention (CDC) also use the NOAA forecasts for applications with wildfire, health and smoke vulnerability assessments. Exposure to fine particulate matter, i.e., aerosol particles with diameters of 2.5 μm and smaller ($PM_{2.5}$), is recognized as a major health concern and the associated mortality rate is estimated to be higher than the five specific causes of death examined by the global burden of disease [GBD, Burnett et al., 2018].

The role of aerosols in Numerical Weather Prediction (NWP), through interaction with atmospheric radiation and precipitation physics (direct, semidirect, and indirect effect), and their impact on meteorological fields in both weather and climate scale, have been widely recognized in many studies [e.g. Fast et al. 2006, Levin and Cotton, 2009; Chen et al., 2011; Grell et al. 2011; Forkel et al. 2012; Muhlbauer et al., 2013; Xie et al., 2013; Yang et al., 2014; Wang H. et al., 2014, Wang Q. et al., 2014]. For example, global and regional models established a connection between dust emissions and weather patterns over synoptic-to-seasonal time scales [Haustein et al., 2012; Zhao et al., 2010]. Results from NASA's Goddard Earth Observing System (GEOS-5) forecasting system showed that the net impact of the interactive aerosol associated with a strong Saharan dust outbreak resulted in a temperature enhancement at the lofted dust level and a reduction near the surface levels, which improved forecasts of the African easterly jet (AEJ) [Reale et al., 2011]. Furthermore, the microphysical and thermodynamic effects from aerosols may play a role in impacting development of tropical cyclones [Rosenfeld et al. 2012].

Additional studies at operational weather centers indicate the importance of including aerosol feedback in NWP for operational forecasting. The inclusion of the direct and indirect effects of aerosols in the global NWP configuration of the Met Office Unified Model (Met UM) indicated that using prognostic aerosols led to better temporal and spatial variations of atmospheric aerosol optical depth (AOD) and was of particular importance in cases of large sporadic aerosol events such as large dust storms or forest fires [Mulcahy et al., 2014]. At ECMWF, Rodwell and Jung [2008] showed an improvement in forecast skill and general circulation patterns in the tropics and extra-tropics by using a monthly aerosol climatology rather than a fixed climatology in the ECMWF global forecasting system. Later on, ECMWF replaced the aerosol climatologies with aerosols from a reanalysis of atmospheric composition produced by the Copernicus Atmosphere Monitoring Service [Bozzo et al, 2020]. At National Centers for Environmental Prediction (NCEP), the operational RAPid refresh (RAP) and High-Resolution Rapid Refresh (HRRR) storm scale modeling systems now include the impact of aerosols from biomass burning emissions on radiation. Due to the importance of aerosol feedback in NWP, the performance of predicted aerosols and their optical properties are critical before implementing the aerosol direct and semi-direct effect in NWP.

NCEP, in collaboration with the NASA/Goddard Space Flight Center (GSFC), developed the NEMS Global Forecast System (GFS) Aerosol Component version 1 (NGACv1) for predicting the distribution of global atmospheric aerosols [Lu et al., 2010].

NGAC is an interactive atmospheric aerosol forecast system with the NEMS global spectral model (NEMS GSM) as the atmosphere model and GOCART as the aerosol model [Wang et al., 2018]. NGACv1 was implemented in 2012 and provided the first operational global dust aerosol forecasting capability at NCEP [Lu et al., 2016]. In NGACv1 an in-line aerosol module based on the Goddard Chemistry Aerosol Radiation and Transport (GOCART) model from GEOS-5 [Chin et al., 2000], but limited to dust only, was used. The NGACv1 used the Earth System Modeling Framework (ESMF) to couple the aerosol module with the GFS. Later on, NCEP implemented a multispecies aerosol forecast capability NGACv2, based on NGACv1 through collaborations among NCEP, NASA/GSFC, the NESDIS Center for Satellite Applications and Research (STAR), and the State University of New York at Albany [Wang et al., 2018].

In July 2016, NOAA took a significant step toward developing a state-of-the-art global weather forecasting model by announcing the selection of a new dynamic core developed at NOAA Geophysical Fluid Dynamics Laboratory (GFDL) to upgrade the GFS. The GFDL Finite-Volume Cubed-Sphere Dynamical Core (FV3) replaced the spectral GFS core in June of 2019 to drive global NWP systems with improved forecasts of severe weather, winter storms, and tropical cyclone intensity and track. NOAA is now on the way to integrate various operational applications into the Unified Forecast System (UFS), a comprehensive, community-based coupled Earth modeling system, designed as both a research tool and the basis for NOAA operational forecasting applications.

Here we describe a new aerosol model component developed through collaborative efforts among the Global Systems Laboratory (GSL), the Chemical Science Laboratory (CSL), and the Air Resources Laboratory (ARL), Environmental Modeling center (EMC) and STAR. This aerosol component was implemented operationally on September 2020 to provide five-day global aerosol forecasts with ~ 25 km horizontal resolution and 64 vertical layers from the surface to 0.2 hPa as one member of the Global Ensemble Forecast System of version 12 (GEFSv12): GEFS-Aerosols v1. The aerosol component is designed as an independent model component for the NOAA Environmental Modeling System (NEMS) framework and includes a coupling interface based on the National Unified Operational Prediction Capability (NUOPC) Layer for model interoperability. All chemistry, aerosol, and emission modeling processes reside and run within this model component. There is not aerosol feedback on the atmospheric model of GEFS, and the aerosols are not in any way interactive with the radiation and clouds. GEFS-Aerosols shows a substantial improvement for both composition and variability of aerosol distributions over those from the previous global aerosol prediction system NGAC. The model predicted global aerosol products from GEFS-Aerosols are also used for other applications, such as to provide lateral boundary conditions for NOAA's regional National Air Quality Forecast Capability (NAQFC), satellite sea surface temperature (SST) physical retrievals, and the global solar insolation estimation [Wang et al., 2018].

The current study presents the development of GEFS-Aerosols and evaluations of its performance in real time and retrospective experiments. Section 2 describes the coupling components of the GEFS-Aerosols member, including the atmospheric component of FV3GFS model, the aerosol component, and the observation, reanalysis, and model data used for evaluation and comparison. The emission inventories of both anthropogenic emission and biomass burning emissions and other chemical input data are presented in Section 3. Section 4 and Section 5 are the evaluations of Day-1 real-time forecast since July 2019

and the Day-1 retrospective forecast for the ATom-1 periods of 2016 summer, respectively. The conclusions and future plans are summarized in Section 6.

2. Model and data

2.1 Descriptions of GEFS-Aerosols

2.1.1 FV3GFS

The global Finite-Volume cubed-sphere dynamical core (FV3) developed by GFDL was chosen by NOAA as the non-hydrostatic dynamical core to be the Next Generation Global Prediction System (NGGPS) of the National Weather Service in the US [Black et al., 2021]. Currently the FV3 was successfully implemented within the physical scheme of GFS, and the FV3-based GFS version 15 (GFSv15) became operational on June 2019, providing the metrological basis for coupling with a simple aerosol prediction component. The GEFS is a weather forecast modeling system made up of 31 separate forecasts, or ensemble members, which have the same horizontal (~25 km) and vertical resolution (64 layers from the surface to 0.2 hPa). The GEFS-Aerosols is only using one of the same weather model as other GEFS members but includes the prognostic aerosols. It is about 2.5 times computational cost when include the aerosol component in the forecast. In the operation, there is no execution time since the it only performs 120 hours forecast with aerosol component, while other members without aerosol component would perform 384 hours forecast. The NCEP started the GEFS to address the nature of uncertainty in weather observations that are used to initialize weather forecast models and uncertainties in model representation of atmospheric dynamics and physics. The aerosol component coupled with FV3GFS v15 has been merged into the GEFS, as a single ensemble member named GEFS-Aerosols, for real-time and retrospective forecast that preceded operational implementation, which occurred in September 2020.

All sub-grid scale transport and convective deposition related to aerosol is handled inside the atmospheric physics routines of simplified Arakawa–Schubert (SAS) scheme, which required consistent implementation of positive definite tracer transport and wet scavenging in the physics parameterizations GFSv15 and subsequent in the forecast system of GEFSv12.

2.1.2 Aerosol component

The current aerosol component in the GEFS-Aerosols model is based on the simple bulk aerosol modules from WRF-Chem [Grell et al., 2005; Powers et al., 2017], and the first time to be used in the global model is the Flow-following finite-volume Icosahedral Model (FIM), as FIM-Chem [Zhang et al, 2022], including aerosol modules from GOCART. The metrological fields (such as land use and other climatological surface fields, vegetation type etc.) are imported from the FV3 atmospheric model to the chemical model to drive the aerosols components. They are consistent in the FV3 atmospheric model and chemical model. Other than the aerosols convective wet scavenging, all the chemical related processes of source and sink, such as emission, dry deposition, settling, large-scale wet deposition, chemical reactions are handled by the chemical model. The large-

scale wet deposition and dry deposition modules are from WRF-Chem for GOCART aerosols scheme, which are column model driven by meteorological input from atmospheric model. Large-scale wet removal of aerosols includes below-cloud removal (washout) following Easter et al. [2004] and the details of below-cloud wet scavenging via interception and impaction can be found in Slinn [1984]. The dry deposition is the same as Chin et al. [2002]. After updating the chemical tracers in chemical model, they are passed back to FV3 atmospheric model for transport and advection.

The GOCART aerosol modules use simplified sulfur chemistry for sulfate simulation, bulk aerosols of black carbon (BC), organic carbon (OC), and sectional dust and sea salt [Chin et al., 2000]. For OC and BC, the hydrophilic and hydrophobic components are considered and the chemical reactions for gaseous sulfur oxidations are calculated using prescribed OH, H_2O_2, and NO_3 fields for gaseous sulfur oxidations [Chin et al., 2000]. The GOCART model background fields of prescribed OH, H_2O_2, and NO_3 have been replaced by the newer version of 2015 from the NASA GEOS Global Modeling Initiative (GMI) Chemical transport model (https://acd-ext.gsfc.nasa.gov/Projects/GEOSCCM/MERRA2GMI/). These are monthly mean data and these prescribed OH, H_2O_2, and NO_3 fields would not be transported and changed in space. The marine dimethyl sulfide (DMS) emission is calculated as a product of sea water DMS concentration and sea-to-air transfer velocity as described by Chin et al., [2000]. Recently, some modifications and updates have been implemented, including the biomass burning plume rise module adapted from High-Resolution Rapid Refresh (HRRR)-Smoke based on WRF-Chem, the capabilities of using the biomass-burning emission calculations based on the Blended Global Biomass Burning Emissions Product version 3 (GBBEPx v3] [Zhang et al., 2014] emission and Fire Radiative Power data provided by NESDIS as well as the application of the global anthropogenic emission inventories from Community Emissions Data System (CEDS).

The sea salt scheme was updated to the most recent version with five size bins based on NASA's 2nd-generation GOCART model (Colarco et al., 2010). The model has the capable of handling volcanic eruptions, which need the estimate of injection height and SO_2 and volcanic ash emissions. While for the predicted results in the paper, the volcanic emission has not been included.

A new dust emission scheme, referred to as FENGSHA, was implemented in GEFS-Aerosols. The scheme, which is also used in NOAA's National Air Quality Forecast Capability, is modified from the original Owen equation [Tong et al., 2017, Owen, 1964; Shao et al., 1993],

$$\mathrm{F} = \sum_{j=1}^{N} K \times A \times \frac{\rho}{g} \times S \times u_* \times \left(u_*^2 - u_{*tj}^2\right) \quad \text{for } u^* > u^*t_j \quad (1)$$

where N is the number of soil types in a particular grid cell, K is the ratio of vertical to horizontal emission flux, A represents particle supply limitation (availability), ρ is air density, g is gravitational acceleration, S is the soil erodibility potential, u^* is friction velocity, and u^*_{tj} is the threshold friction velocity for soil type j [Shao et al., 1993]. Dust emission is calculated only when friction velocity exceeds the designated threshold value for the land use type and soil texture. The threshold friction velocities are based on wind tunnel measurements done in both the laboratory and field [Gillette et al., 1980].

What makes FENGSHA unique is the way in which the threshold values are determined. Unlike models based on Marticorena and Bergametti [1995] or Shao et al., [2011], threshold values are based on surface and wind tunnel flux measurements of

saltation [Gillette, 1988]. The drag partition in the FENSGHA scheme is described by the MacKinnon et al. [2004] parametrization using the model surface roughness (z0) or derived from the surface roughness estimates using the Advanced Scatterometer (ASCAT) as described by Prigent et al. [2012]. The Fécan et al [1998] soil moisture correction is used to adjust the dry threshold friction velocity. Once the total windblown dust emission flux is computed the total flux is distributed into the modeled dust bins using the Kok [2011] distribution.

A new sediment supply map, the Baker-Schepanski Map (BSM), which was developed from the ideas of Chappell and Webb [2016] is currently used within the GEFS-Aerosol FENGSHA implementation. Chappell and Webb [2016] created an approach similar to that of the Raupach [1992] model for lateral cover but instead uses a top-down view to describe the area of the turbulent wake using an analogous shadow instead of a two-dimensional view. The shadow approach is sensitive to the configuration of the roughness elements meaning that it is sensitive to the placement of the roughness elements in relation to each other. The BSM describes the probability of momentum mixing directly to the soil surface through the canopy. For the application into GEFS-Aerosols a monthly 3-year climatology of the BSM was created which refers to a monthly average over 3 observation years, in this case 2016, 2017 and 2018 as these were the latest full years at the time of model development.

2.1.3 GEFS-Aerosols coupled architecture, running sequence and forecasting workflow

The aerosol component of GEFS-Aerosols couples directly to the FV3-based atmospheric component via the NUOPC Layer [Theurich et al., 2016], which is the foundation of NOAA's modeling framework (Fig. 1). Fig. 2a shows the model coupled structure that the aerosol component imports meteorological fields from the atmospheric model and exchanges aerosol mixing ratios at each coupling time step via standard NUOPC connectors. Each aerosol species is simulated as a prognostic atmospheric tracer, which is advected by the FV3 dynamical core and undergoes convective mixing and PBL diffusion within the atmospheric physics. All aerosol composition and emission-related processes are computed in GEFS-Aerosols after the atmospheric physics has been advanced and passed to the chemical model following the sequences as emission, settling of dust and sea salt, plume-rise of fire emission, dry deposition, large-scale wet deposition, chemical reactions and carbonaceous aerosol updating. Tracer mixing ratios are then updated and exported back to the atmospheric model.

Bundling all aerosol composition processes in a single model component led to the implementation of a sequential coupling scheme with the atmospheric component. At each coupling time step, the atmospheric dynamical core and physics processes (including radiation) are computed first. The aerosol component is then executed to perform all air composition processes and transfer the updated tracers back to the atmospheric component. Finally control returns to the atmospheric model, which updates the atmospheric state with new meteorology and aerosols concentrations. To minimize overhead associated with data exchange between model components, GEFS-Aerosols is run on the atmospheric grid, which is imported from the atmospheric component through NUOPC. Additionally, the coupling run sequence assigns to the aerosol component the identical set of Persistent Execution Threads (PETs) used by the atmospheric model's forecast component. This allows the model to leverage NUOPC's ability to access coupling fields by memory reference, minimizing the memory footprint for the coupled system.

The sequence of steps involved in moving from the beginning to the end of a forecast process is controlled by the workflow. In a retrospective or real time forecast, the chemical tracers are cycled from the output of a previous forecast as the initial condition. In operation, the computational cost with aerosol component would take 129 mins for 120 hours forecast. Therefore, the efficiency is about 2.53 times computational cost by including aerosol component compared to the one without aerosol component in the forecast. The workflow shown in Figure 2(b) describes the steps including pre-processing (prepare input data) and post-processing (process output data) before and after forecast for the GEFS-Aerosols in the forecast system. This initial implementation of GEFS-Aerosols does not include aerosol data assimilation, so the chemical tracers in the restart files are used as the chemical initial condition for the next forecast. The yellow box includes the tasks/steps for atmospheric mode, while the green box includes the tasks/steps for chemical model. The AOD is calculated in the post-processing part of the workflow, using a look-up table (LUT) of aerosol optical properties from NASA GOCART model [Colarco et al. 2010, Colarco et al. 2014], which was implemented in the Unified Post Processor (UPP, https://dtcenter.org/community-code/unified-post-processor-upp). It should be noted that the LUT reflects the impacts of a larger number of aerosol species in the atmosphere than the simple GOCART module treats. Also, considering the bulk aerosol scheme in GOCART, there is no size distribution for OC, BC and sulfate, the LUT may have uncertainties in the AOD calculation. Based on observational validation, some adjustments with factor of 2 have been applied in into LUT calculation to compensate the contributions for the absence of nitrate, ammonium and secondary organic aerosol (SOA) in GOCART.

2.2 Observation, reanalysis data and other model data

The real-time forecast experiments were evaluated using the following ensemble analysis, reanalysis data, satellite and in situ observational data, aircraft measurements, and model predictions. We compare each day model forecast hours with same day reanalysis or analysis data and compute the AOD statistics (e.g. bias, RMSE, correlation etc.) for each grid for each pair of model and reanalysis or analysis data for that model forecast hour. We then calculate that for the entire 4 months of the study period and averaged it over the entire 4 months for each grid points. This method gives an overall estimate of systematic bias of the model in spatial and temporal scale.

2.2.1 Reanalysis data of AOD

1) Total AOD instantaneous reanalysis dataset from the second Modern-Era Retrospective analysis for Research and Application [MERRA-2, Gelaro et al., 2017]. The MERRA-2 reanalysis provides various AOD product at 0.625 x 0.5 degree horizontal resolution and at 72 vertical levels. MERRA-2 reanalysis data is not synchronous as real-time, and normally has 1-2 months' time lag.

2.2.2 Observation data of Satellite AOD, AERONET AOD and ATOM-1 concentration.

1) MODIS provides near-global coverage of aerosol measurements in space and time. We have used a MODIS Level-3 (daily and monthly at 1 degree horizontal resolution) AOD dataset in this study (https://ladsweb.nascom.nasa.gov/). The dataset belongs to the Collection 6.1 combined land and ocean from the Aqua satellite [Levy et al., 2013]. This

latest collection of MODIS data includes AOT data based on refined retrieval algorithms, in particular the expanded Deep Blue algorithm [Hsu et al., 2013; Sayer et al., 2013]. It introduces a merged AOD product, combining retrievals from the Dark Target (DT) and Deep Blue (DB) algorithms to produce a consistent data set covering a multitude of surface types ranging from oceans to bright deserts [Sayer et al., 2014]. In this work the aerosol product Dark_Target_Deep_Blue_Combined_Mean was used for quantitative evaluation of model results. We have used Collection 6.1 MODIS AOD at 550nm, which has Expected Errors (EEs) of [± (0.05 + 15%AOD)] and [± (0.03 + 5%AOD)] for Dark Target retrievals at a 10-km resolution over land and ocean, respectively. The EEs are approximately [± (0.03+21%AOD] for 'arid' and [± (0.03+18%AOD)] for 'vegetated' path Deep Blue retrievals at a 10-km resolution over land [Levy et la., 2013].

2) The Visible Infrared Imaging Radiometer Suite (VIIRS) sensor onboard the Suomi National Polar Orbiting (S-NPP) satellite provides sets of aerosol environmental data records (EDRs) based on daily global observations from space [Jackson et al., 2013; Liu et al., 2013]. Beginning in 2012, VIIRS provides AOT at 550 nm at a global 0.25 degree horizontal resolution. Daily gridded Enterprise Processing System (EPS) VIIRS data used are from the NOAA STAR ftp site at ftp://ftp.star.nesdis.noaa.gov/pub/smcd/VIIRS_Aerosol/npp.viirs.aerosol.data/epsaot550/.

3) The Aerosol Robotic Network (AERONET), which is a global ground-based network of automated sun-photometer measurements, provides AOT, surface solar flux and other radiometric products [Holben et al., 1998]. It is a well-established network of over 700 stations globally and its data are widely used for aerosol-related studies [Zhao et al., 2002]. AERONET employs the CIMEL sun–sky spectral radiometer, which measures direct sun radiances at eight spectral channels centered at 340, 380, 440, 500, 675, 870, 940 and 1020 nm. AOT uncertainties in the direct sun measurements are within ±0.01 for longer wavelengths (longer than 440 nm) and ±0.02 for shorter wavelengths [Eck et al., 1999]. Table 1 lists number of stations, their location in terms of latitude and longitude. The stations are selected based on years in service and geographic location near the aerosol source regions. Stations covered major aerosol sources: African Dust, Southern Africa and South America (major forest fire stations), mixed aerosol regimes (urban areas in Europe, Asia and N. America), high latitude stations (capture major transport of forest fires from Siberia and Canada).

4) The Atmospheric Tomography Mission (ATom) studies the impact of human-produced air pollution on greenhouse gases and on chemically reactive gases in the atmosphere [Wofsy et al., 2018]. ATom deploys instrumentation to sample atmospheric composition, profiling the atmosphere in 0.2 to 12 km altitude range. Flights took place in each of 4 seasons over a 22-month period in 2016 through 2018. They originated from the Armstrong Flight Research Center in Palmdale, California, flew north to the western Arctic, south to the South Pacific, east to the Atlantic, north to Greenland, and returned to California across central North America over the Pacific and Atlantic oceans from ~ 80°N to ~ 65°S. In August 2016, PALMS was sampling on the NASA DC-8 aircraft as part of the ATom program (https://espo.nasa.gov/missions/atom/content/ATom). Aerosol composition determinations using the PALMS instrument during ATom-1 have been described and interpreted previously [Murphy et al., 2018, 2019; Schill et al.,

2020; Bourgeois et al., 2020]. The PALMS mass concentrations for various species are derived by normalizing the fractions of particles of each size and type to size distributions measured by optical particle counters [Froyd et al., 2019].

2.2.3 Model ensemble analysis AOD and other model forecasts

1) International Centers for Aerosol Prediction - Multi-Model Ensemble (ICAP-MME) provides daily 6-hourly forecasts of total and dust AOD globally out to 120 h at 1 degree horizontal resolution [Reid et al., 2011; Sessions et al., 2015; Xian et al., 2019]. Total AOD in ICAP-MME is provided by the four core multispecies models: the European Centre Medium Range Weather Forecasts Copernicus Atmosphere Monitoring Service (ECMWF-CAMS), the Japan Meteorological Agency Model of Aerosol species in the Global Atmosphere (JMA-MASINGAR), the NASA Goddard Earth Observing System Version 5 (NASA-GEOS-5) and the Naval Research Lab Navy Aerosol Analysis and Prediction System (NRL-NAAPS) modeling systems. Dust-only AOD is provided by the aforementioned four models, plus the Barcelona Supercomputer Center Chemical Transport Model (NMMB/BSC-CTM), the United Kingdom Met Office Unified Model (UKMO-UM) and NGACv2. However, the NGACv2 is only used for dust AOD in ICAP-MME, not use to compute ensemble mean in ICAP-MME for total AOD. All four of the multispecies models incorporate aerosol data assimilation (DA) and satellite-based smoke emissions. ICAP-MME is able to provide real-time comparison for synchronous evaluation of operational forecast. The correlation and RMSE between ICAP-MME and AERONET indicating in Table 1 shows that ICAP analysis is quite close to observation, which is good to use it as the global evaluated data, especially when the MERRA-2 data is not available in the real-time or operational forecast.

2) The NEMS GFS Aerosol Component Version 2.0 (NGACv2) for global multispecies aerosol forecast developed by NCEP and collaborators was previously used to provide operational global multispecies aerosol forecasts at NCEP [Wang et al., 2018]. The anthropogenic emissions are based on EDGAR V4.1 [Janssens-Maenhout, 2010] and AeroCom Phase II [Diehl et al., 2012]. The smoke emissions are from NESDIS STAR's GBBEPx, blended from the global biomass burning emission product from a constellation of geostationary satellites [GBBEP-Geo, Zhang et al., 2012; Zhang et al., 2014] and GSFC's Quick Fire Emission Data Version 2 from a polar-orbiting sensor [QFED2, Darmenov and da Silva, 2015]. NGACv2 uses the same physics package as the 2015 version of the operational GFS. NGACv2 included additional aerosol species of sea salt, sulfate, organic carbon, and black carbon from the updated GOCART modules. Both science and software upgrades in the global forecast system were updated and implemented into NGACv2 in March 2017 to provide 5-day multispecies aerosols forecast products at the T126 L64 resolution, approximately 100 km. The comparison of model configurations for GEFS-Aerosols and NGACv2 has been shown in Table 2 based on the model information from Wang et al. [2018].

3. Emissions

3.1. Anthropogenic emissions and background fields

The preprocessor PREP-CHEM-SRC v1.7, a comprehensive tool that prepares emission fields of trace gases and aerosols for use in atmospheric chemistry transport models, was used to generate the anthropogenic emissions, background fields of OH, H_2O_2, NO_3, DMS and dust scheme input of clay and sand at the FV3 grid resolution for GEFS-Aerosols [Freitas et al., 2011]. Two global anthropogenic emission inventories were chosen as input to drive the model, both providing monthly emissions. One is from the Community Emissions Data System (CEDS), which provides the emissions of BC, OC and SO_2 in 2014 with 0.5 degree horizontal resolution [Hoesly et al., 2018]. The CEDS inventory improves upon existing inventories with a more consistent and reproducible methodology applied to all emission species, updated emission factors, and more recent estimates in 2014. The data system relies on existing energy consumption data sets and regional and country-specific inventories to produce trends over recent decades [Hoesly et al., 2018]. The Hemispheric Transport of Air Pollution (HTAP) version 2 [Janssens-Maenhout et al., 2015] inventory provides the emissions of BC, OC SO_2, $PM_{2.5}$ and PM_{10} in 2010.

Figure 3 shows the comparisons of anthropogenic emissions between CEDS and HTAP for SO_2, BC and OC in July. Aside from the shipping lanes showing up in CEDS, there is generally broader spatial coverage in CEDS. For SO_2, the CEDS emissions are much larger over the eastern US, eastern China and Europe. Much higher values of BC and OC are seen in CEDS over Eastern Asia, South Asia and Europe. Similarly, much larger values for BC and OC are seen in the Southern Hemisphere in CEDS. We performed experiments by comparing model predictions using these two different anthropogenic emissions datasets with ATom-1 observations (figures not shown here). Slight improvements in SO_2 correlations and bias are seen and the sulfate, OC and BC biases improve over the Atlantic Ocean when using the CEDS emissions in comparison with the HTAP dataset. It should be noted that these anthropogenic emissions data are not impossible to catch up the date of real-time forecast. And it normally has time lag and represents the emissions of a different previous years. The inconsistency may have some impact on the predictions in 2019. But that is the most recently available version of anthropogenic emission. It well known that strong actions have been taken to improve the worsening atmospheric environment and decrease the emission over China in the last 10 years [Chen et al., 2017; Zhang et al., 2012; Liu et al., 2016]. Considering the decreasing emission trend over China, the CEDS 2014 anthropogenic would result in some overprediction after 2014.

We validated the GOCART background fields of OH and H_2O_2 against the ATom-1 observations. Even though these background fields are model-derived climatologies, they both compare very well with the ATom-1 measurements. The newer NASA GEOS/GMI fields show improvement in the model-measurement biases for both OH and H_2O_2.

3.2 Biomass burning emission

The operation of GEFS-Aerosols is using the GBBEPx v3 emission with Fire Radiative Power (FRP). The GBBEPx v3 system produces daily global biomass burning emissions of $PM_{2.5}$, BC, CO, CO_2, OC, and SO_2) by blending fire observations from MODIS Quick Fire Emission Dataset (QFED), VIIRS (NPP and JPSS-1) fire emissions, and Global Biomass Burning Emission Product from Geostationary satellites (GBBEP-Geo). GBBEP-Geo also produces hourly emissions from

geostationary satellites, at individual fire pixels. In the results shown here, GBBEPx daily biomass burning emissions on the FV3 C384 global grid are used for GEFS-Aerosols. The details of the GBBEPx v3 algorithm can be found in https://www.ospo.noaa.gov/Products/land/gbbepx/docs/GBBEPx_ATBD.pdf.

A one-dimension (1-D) time-dependent cloud module from High-Resolution Rapid Refresh (HRRR)-Smoke model has been implemented into GEFS-Aerosols to calculate injection heights and emission rates online [Freitas et al., 2007]. The new scheme in HRRR-Smoke is a modified version of the 1D plume rise scheme used in WRF-Chem [Freitas et al., 2007]. The new plume rise scheme is using the FRP data instead of the look-up table to estimate the fire heat fluxes [Ahmadov et al, 2017]. The 1-D cloud module is able to be applied with these two different fire emissions datasets to account for plume-rise that distributes the fire emissions vertically and better simulate the fire events and pollution transport of smoke plumes.

To validate model performance when using the GBBEPx v3 fire emissions with a plume-rise module based on real-time FRP data, we compare the real-time GEFS-Aerosols AOD with other reanalysis data, satellite observations and the NGACv2 model for the big fire event in August 2019. Smoke from large fires burning in the Amazon rainforest, primarily in Brazil, Bolivia, Paraguay, and Peru, stretched over northern South America in mid-August. Figure 4 shows the total AOD forecast on 25th August compared against the NGACv2 model, MERRA-2 reanalysis data and satellite observations of VIIRS and MODIS. For both satellites, daily gridded AOD is used to compare against the model forecast at 18z. The GEFS-Aerosols AOD is able to reproduce the enhanced AOD due to several fire events over South America near the border of Bolivia, Paraguay, and Brazil, which were also observed by the VIIRS and MODIS satellite instruments and captured by the MERRA2 analysis. Although there are a lot of missing data downwind from the fires in the satellite observations of VIIRS and MODIS, especially over the south Pacific, GEFS-Aerosols and MERRA-2 results are consistent in showing the transport of fire plumes into the tropical Pacific and southern Atlantic. In contrast, the NGACv2 model does not capture these fire events, and exhibits only a very slight AOD enhancement. NGACv2 AOD is more than 80% smaller than the observations over the fire source region and produces little or no transported smoke over the surrounding areas.

Beyond the fires burning in South America, an even greater number of blazes on the African continent are observed by the satellite images at almost the same time in August 2019. Angola experienced almost three times more fires than Brazil in the middle of August 2019. There were around 6,000 fires in Angola, more than 3,000 in Congo and just over 2,000 in Brazil, according to NASA satellite imagery (https://earthobservatory.nasa.gov/images/145421/building-a-long-term-record-of-fire). One of the main large-scale aerosol features of Sub-Saharan Africa is the June-to-September biomass burning season in Angola, Congo, and Zambia [Bauer et al., 2019]. Overall, the GEFS-Aerosols model reasonably simulates the major burning event on August 25th, 2019 over southern Africa (Figure 4), but overestimates the central African plume when compared with the MERRA2 analysis. The satellite AOD retrievals of VIIRS and MODIS off the coast of central Africa are challenging due to screening by the stable stratiform cloud deck over the ocean that occurs during the fire season, creating less reliable coverage from these observational data. Nevertheless, we can still see consistent AOD enhancements over the fire source regions and surrounding areas for both GEFS-Aerosols and the observations. NGACv2, however, is quite different from the satellite

observations and MERRA2 analysis, underestimating the AOD more than 50-90% percent over the southern Africa fire source region and showing little obvious enhancement.

Future work will explore the use of diurnal fire profiles based on historic GOES fires products applied to estimate biomass burning emissions to enhance forecast behavior. Additionally, a parameterization based on fire weather index (FWI) to estimate biomass burning emissions on longer temporal scales may help to improve and extend the forecast of fire impacts.

4. Real-time forecast Evaluation

4.1 Evaluation of global AOD

A real-time forecast was performed starting on July 1 2019 on ~25km resolution and continuing to the present day using the GBBEPx v3 fire emissions with the plume-rise module based on real-time FRP data.

We evaluated the GEFS-Aerosols model performance with the daily AERONET data globally. The locations of the 60 selected AERONET sites where these comparisons were made are listed in Table 1. It also indicates the correlation and root mean square error (RMSE) of GEFS-Aerosols, ICAP and NGACv2 AOD with respect to that of AERONET observation. The GEFS-Aerosols, NGACv2 and ICAP predictions are sampled at the same locations as the AERONET sites for these comparisons. The left panel in Figure 5 (a and b) shows the correlation coefficients between daily total AOD observed by AERONET and the day 1 forecast of model AOD from GEFS-Aerosols and NGACv2 for the period between 7/5/2019 and 11/30/19. The correlation coefficients range from 0.5 to 0.9 for GEFS-Aerosols at most sites, except for several sites in South America, Africa and eastern Asia near fire source regions, which are slightly lower than those of the ICAP. In contrast, the correlation coefficients of daily total AOD between the NGACv2 and AERONET observations are lower than 0.5 globally, even ranging from 0.1 to 0.3 at most sites. A more quantitative display of correlation coefficients for a selection of 60 AERONET sites for GEFS-Aerosols and NGACv2 is presented in Table 1. This comparison strongly indicates the improved performance of total AOD daily variation in GEFS-Aerosols prediction when compared with NGACv2. There are 20 sites (about 30% of total sites) displaying highly correlated total AOD for the AERONET data and GEFS-Aerosols, with the correlation coefficients exceeding 0.7. In contrast, there is only 1 site with a correlation coefficient larger than 0.7 for NGACv2 model vs. AERONET, and 19 sites have correlation coefficients that are less than 0.2 for AERONET and NGACv2. Fig. 5 c and are the RMSE of GEFS-Aerosols and NGACv2 with respect to AERONET observation. Most of RMSE values are below 0.25 in GEFS-Aerosols over North America, Europe and Africa. However, the RMSE values in a lot of sites over Africa and Asia are above 0.3 in NGACv2. From Table 1, the ICAP results show the best performance in both the correlation and RMSE.

In addition to comparing with the AERONET data, Fig. 6 shows the Day 1 AOD prediction of GEFS-Aerosols and NGACv2 compared with the MERRA-2 reanalysis and MODIS observations averaged from July to November 2019. The GEFS-Aerosols prediction is able to capture the geographical features of AOD as represented by the MERRA-2 reanalysis data and MODIS satellite observations, such as the dust plumes over North Africa and the Arabian Peninsula, biomass burning plumes in southern Africa, south America, northwestern America and eastern Europe, polluted air over eastern and southern Asia, and

high-latitude sea-salt bands over the southern hemisphere. The high AOD over southern Africa and northern India is more comparable to the MODIS observation. As pointed out by Bhattacharjee et al. [2018], the NGACv2 predictions exhibit widespread underestimates over most of these high AOD regions, such as eastern Asia, and fire source regions of southern Africa, eastern Europe, southeastern Asia.

Figure 7 indicates the Day 1 AOD forecast biases of GEFS-Aerosols and NGACv2 with respect to MERRA-2 reanalysis between 7/5/2019 and 11/30/19 for dust, OC and sulfate. The predicted dust AOD in GEFS-Aerosols is quite comparable to that of MERRA-2 results, with only small negative biases of ~0.08 over Asia and the downwind areas of African dust source regions of Atlantic and south Asia (Figure 8a). GEFS-Aerosols has some small positive biases relative to MERRA-2 of ~0.1 over Australia (in red). In contrast, dust AOD in NGACv2 (Figure 8b) shows large over predictions of MERRA-2 over Africa with maximum value ~ 0.45 and about 0.02-0.05 over large areas of Asia and North Pacific and North America. Wang et al. [2018] also showed that the predicted dust AOD in NGACv2 over northwestern Africa is much larger than GEFS-Aerosols, MERRA-2 and MODIS observations.

OC is a major component emitted from wildfires, and OC AOD is a good indicator of the performance of fire impacts. GEFS-Aerosols OC AOD shows smaller biases compared to the MERRA-2 reanalysis than those of NGACv2 (Figure 7c and d). Positive biases in GEFS-Aerosols OC AOD of less than 0.2 occur mainly over southern Africa, eastern Asia, south Asia and the Middle East. The GEFS-Aerosols overprediction of OC AOD compared with MERRA-2 over eastern China may be associated with the overestimate of anthropogenic emissions by using CEDS 2014, since this is not a major fire source region. GEFS-Aerosols shows small negative biases, of less than 0.1, over South America and middle and eastern Europe. Overall, the biases of OC AOD in NGACv2 relative to MERRA-2 are dominated by under prediction globally with the largest biases of more than 0.3 over major fire source regions of southern Africa, the Amazon region of South America, Southeastern Asia and Sibera (Figure 7d).

For sulfate AOD, the GEFS-Aerosols forecast over predicts MERRA-2 by ~0.08 over eastern Africa, the Middle East, and southeastern China, where SO_2 anthropogenic emissions are dominant. Small GEFS-Aerosols under predictions, less than 0.1 AOD, are seen over broad areas of the Northern Hemisphere, such as eastern North America and its downwind areas over the north Atlantic and western Europe, as well as eastern Asia and its downwind areas (Figure 7e). As in the case of OC AOD, the global sulfate AOD in MERRA-2 is under predicted significantly by NGACv2 (Figure 7f). The areas with the largest NGACv2 vs. MERRA-2 sulfate bias are mainly over the major anthropogenic source regions, such as India and eastern China, where the underestimates exceed 0.18, and in the eastern US and western Europe, where they exceed 0.1.

The summary comparison of the GEFS-Aerosols and NGACv2 Day 1 total AOD prediction biases with respect to MERRA-2 reanalysis between 7/5/19 and 11/30/19 is shown in Figure 8. Generally, the GEFS-Aerosols model is able to reproduce the total AOD very well, much better than NGACv2 (see Figure 8a and b). The GEFS-Aerosols over predictions over eastern China and Southern Hemisphere (~0.2-0.3) are mainly due to anthropogenic OC and SO_2 for the former and fire emissions of OC for the latter, respectively. Both GEFS-Aerosols and NGACv2 total AOD have small negative biases (~0.1) relative to MERRA-2 over the northwestern China dust source region. Negative biases of GEFS-Aerosols vs. MERRA-2 in South

America may be caused by inadequate fire emissions and in Europe that may be related to anthropogenic SO_2 emissions. The spatial locations of biases in GEFS-Aerosols with respect to MERRA-2 reanalysis total AOD (Figure 8a) are similar to the comparisons with the individual aerosol species from MERRA-2 discussed above (Figure 7a, c and e). The NGACv2 total AOD is biased low relative to MERRA-2 almost globally except for the over prediction over North Africa due to dust (Figure 8b). The largest NGACv2 total AOD biases are mainly caused by the under predictions of fires over the fire source regions of South America, southern Africa, Southeastern Asia and middle and eastern Europe and the anthropogenic source regions over eastern China, India and eastern North America, with maximum total AOD biases reaching more than 0.5.

4.2 Evaluation of AOD associated with fire events

We choose some sites near the major fire source region, which have available observation data for the duration of this study and hold long records based on various previous studies. Figure 9 indicates the total AOD time series of AERONET observations compared against ICAP, NGACv2 and GEFS-Aerosols model predictions at the four AERONET sites near the fire source regions of South America during the period of 7/1/19-11/30/19. At the Alta Floresta site, which is in the middle of Amazon fire source region, the daily AOD variations of both the ICAP and GEFS-Aerosols day 1 predictions are quite consistent with that of the AERONET data, especially as they are able to reproduce two peaks in AOD enhancements in late August and late September caused by fire plumes (Figure 9a). The correlation (RMSE) is 0.66 (0.23), 0.9 (0.12) and 0.68 (0.31) for GEFS-Aerosols, ICAP and NGACv2. Obviously, NGACv2 results under predict AERONET observations almost throughout the whole period with a significantly larger bias than GEFS-Aerosols or ICAP, and the two August-September peaks in total AOD enhancements are essentially missed in the NGACv2 prediction.

The Itajuba site is located southeast of the Alta Floresta site and in the downwind areas of the Amazon fire source region. The total AOD time series of GEFS-Aerosols prediction matches closely those of ICAP and AERONET during most of the time period, though there are some discrepancies from the end of August to middle September when the GEFS-Aerosols underpredicts the high AOD episode (Figure 9b). GEFS-Aerosols is able to predict the two AOD enhancements in mid-October and early November, which is quite comparable as ICAP. The correlation (RMSE) is 0.856 (0.15) and 0.936 (0.09) for GEFS-Aerosols and ICAP with respect to AERONET at the site of Itajuba, only 0.451 (0.22) for NGACv2. The NGACv2 prediction also generally underestimates the observations at this site too (Figure 9b). The NGACv2 results are closer to the ICAP, GEFS-Aerosols and AERONET before August, and NGACv2 shows a slight increase of total AOD in early September, but the NGACv2 AOD magnitude is much lower than the AERONET by about a factor of 5-7 from the middle of August onward.

Located in the southern part of the Amazon fire region, the site of Santa Cruz Utepsa is south of the AltaFloresta site. The correlation (RMSE) values of GEFSA-Aerosols and ICAP with respect to AERONET are 0.8 (0.18) and 0.88 (0.13) respectively, which shows better performance than those of NGACv2 with 0.3 (0.39) at this site in predicting the total AOD through the 5 months from July to November (Figure 9c). The model not only reproduces the total AOD temporal variation of the AERONET results, but also captures several fluctuations of high AOD in August and September caused by Amazon fire

events. Again, some of fluctuations in total AOD were captured by the NGACv2 prediction, but the modeled AOD magnitudes are 2-4 times lower than the observations.

The last site of RioBranco is also located in the Amazon fire source region but to the west of the AltaFloresta site. There are some missing data at this site for the AERONET total AOD from middle July to middle September (Figure 9d). During this period, the GEFS-Aerosols prediction is slightly lower than ICAP by about 5-10%. Both ICAP and GEFS-Aerosols total AOD match the AERONET variations well when the AERONET data are available again from mid-September. Several peaks of total AOD are also captured by GEFS-Aerosols in middle September and early November. The NGACv2 prediction shows enhanced total AOD in middle August, with low biases by more than 2-3 times compared to ICAP and GEFS-Aerosols. For other enhancements of total AOD after October, the NGACv2 results completely miss the fire events and do not show any fluctuations. The correlation (RMSE) is 0.80 (0.24) and 0.90 (0.17) for GEFS-Aerosols and ICAP with respect to AERONET at the site of RioBranco, only 0.51 (0.44) for NGACv2.

We also evaluate the total AOD time series of AERONET against ICAP, NGACv2 and GEFS-Aerosols for fire regions of central and southern Africa. The comparisons at seven AERONET sites from July to November are shown in Figure 10. Generally, the GEFS-Aerosols predictions are able to capture the daily total AOD variation measured by AERONET. At the site of Misampfu, the GEFS-Aerosols mode is somewhat better than that of ICAP in predicted the peaks of high AOD. The correlation coefficients at the sites of Maun Tower and Lubango are much high than those of ICAP (see Table 1). While both the GEFS-Aerosols and ICAP overpredicted the total AOD most of time throughout the three months at the station Bamenda located north of the major African fire source region. The NGACv2 total AOD forecast shows under prediction at most of the AERONET sites in this region. Meanwhile, NGACv2 and ICAP predictions are not consistent with AERONET either, especially for several observed high peaks which are not reproduced by the model results (e.g. Gabon). At the remote site of Ascension Island located west of the African fire source region, the GEFS-Aerosols and ICAP are able to capture the AOD enhancements in the middle of August, and shows the best performance of the three different models (see Table 1). For other sites that are located in the fire source region, such as Monguinn, Misamptu, Maun Tower, and Lubango, the prediction of the GEFS-Aerosols model shows higher correlation of 0.68, 0.79, 0.84 and 0.71 than those of NGACv2 as 0.51, 0.26, 0.29, 0.35. The RMSE values of GEFS-Aerosols are 0.18, 0.15, 0. 10. 0.15, which is much lower than the NGACv2 of 0.32, 0.34, 0.23, and 0.32. It suggests that the GEFS-Aerosols better matches the observed temporal variation of total AOD than NGACv2. One peak in early August at the Monguinn site, one peak in middle September at the Misampfu site, two peaks in early August and early September at Maun Tower site and one enhancement in August at Lubango are all predicted by the GEFS-Aerosols model. The ICAP forecasts shows lower biases against the AERONET total AOD for predicting these peaks, while none of these peaks are captured by NGACv2. GEFS-Aerosols shows slight over predictions in mid-July and late August for Gabon and early August for Lubango.

4.3 Evaluation of AOD associated with dust events

Thirteen AERONET sites inside the major dust source regions of western North Africa, Asia and the Middle East and surrounding areas have available data from July to November 2019. The total AOD time series of GEFS-Aerosols, ICAP, and NGACv2 at 6 of these sites are shown in Figure 11. Overall, the GEFS-Aerosols model is able to closely predict the observed total AOD variation, especially at the sites of Banizoumbu, Tenerife, Saada, Ben Salem, Granada and Sede Boker, with much better performance than those of NGACv2 according to the correlation (RMSE) values in Table 1 of GEFS-Aerosols as 0.74 (0.15), 0.77 (0.07), 0.76 (0.14), 0.82 (0.07), 0.85 (0.09), and 0.73 (0.08) verses NGACv2 as 0.33 (0.24), 0.25 (0.18), 0.25 (0.26), 0.25 (0.23), 0.21 (0.16), and 0.19 (0.14) . In addition to NGACv2's overprediction at the sites of Ben Salem and Granada, it does not accurately capture observed temporal variations of total AOD at these sites.

We compare the daily AERONET total AOD with the 1-day forecasts of total AOD from GEFS-Aerosols and NGACv2 at the AERONET sites of Cape Verde, Tamanrassett and Tenerife located in the dust source region over North Africa in Figure 12. The slope of the linear regression of AERONET total AOD vs. GEFS-Aerosols is quite different from that of NGACv2 at the site of Tamanrassett, which is located in southern Algeria and in the middle of the Saharan dust source region. The GEFS-Aerosols linear regression slope is much closer to 1 than that of NGACv2, and the R^2 in the NGACv2 model is lower by a factor of 4 than that of the GEFS-Aerosols model at this site. At the other two sites of Cape Verde and Tenerife, which are in the downwind area west of the African dust source region, the slopes of the linear regressions for GEFS-Aerosols are also much closer to 1 than those of the NGACv2 model. The NGACv2 model, as evidenced by the R^2 values, is more poorly correlated with AERONET than the GEFS-Aerosols prediction. The R^2 values of GEFS-Aerosols is 0.50, 0.33 and 0.59 in these sites, which better captures the dust transport in the downwind areas west of the African dust source region than the NGACv2 model as 0.19, 0.08 and 0.06.

4.4 Evaluation of major regional averages

Figure 13 shows day 1 predictions of total AOD time series by GEFS-Aerosols and NGACv2 compared against the MERRA-2 reanalysis averaged over 9 major global regions from August 2019 to March 2020. The comparison clearly shows the consistency between GEFS-Aerosols and the MERRA-2 reanalysis over most of these 9 regions, especially North Africa, the North Atlantic, Southern Africa, and the South Atlantic, with only minor discrepancies during these 8 months. The total AOD is dominated by dust in North Africa and fire emissions in Southern Africa. The aerosols emitted from dust and fire regions and their long-range transport play important roles in impacting the total AOD over the North and South Atlantic Oceans. The good agreement with MERRA-2 shows that GEFS-Aerosols captures the emissions and transport of dust and fire emissions in these regions.

Total AOD variation in South America is mainly related to biomass burning emissions. GEFS-Aerosols has some slight low biases relative to MERRA-2 from middle September to early October 2019 that are associated with the Amazon fire event. GEFS-Aerosols under predicts MERRA-2 in this region from mid-November 2019 to March 2020, outside the main biomass

burning season, which suggests that the GEFS-Aerosol AOD low biases in this region are mostly associated with sources other than fires.

The European region has the largest differences between GEFS-Aerosols and MERRA-2 reanalysis total AOD among the 9 regions. Although their temporal variations are similar, GEFS-Aerosols under predicts the MERRA-2 total AOD throughout the whole period by a factor of 0.5. The large absolute low biases from August to early October 2019 and March 2020 in Europe which are associated with GEFS-Aerosols underestimates of sulfate AOD (Fig. 8).

From August to early December 2019, the GEFS-Aerosols total AOD looks quite consistent with the MERRA-2 reanalysis on average across East Asia. GEFS-Aerosols high biases starting in middle December 2019 and increasing from January to March 2020 may be associated with the lockdown in China during the Coronavirus disease 2019 (COVID-19) pandemic. Anthropogenic emissions of NO_2, SO_2, VOC, and primary $PM_{2.5}$ over the North China Plain during this period were reduced by 51%, 28%, 67% and 63%, respectively, compared to the previous year, resulting in lower surface aerosol and ozone levels and improvements to air quality [Shi and Brasseur, 2020; Wang and Su, 2020; Xing et al., 2020]. Since the anthropogenic emissions used in GEFS-Aerosols are based on the CEDS 2014 inventory, they definitely overestimate the anthropogenic aerosol emissions during the 2019-2020 lockdown periods.

Both the Eastern and Western US regions exhibit GEFS-Aerosols low biases of about 5-30%, with the largest differences in Eastern US occurring in August 2019. However, the trends of total AOD temporal variations with low in summer and high in winter in the GEFS-Aerosols prediction and the MERRA-2 reanalysis are quite consistent over Eastern and Western US. The minor under predictions by GEFS-Aerosols need further investigation.

In comparison, the NGACv2 predictions show significant under prediction of MERRA-2 total AOD for almost all of these 9 regions throughout this 8-month period. The one exception is North Africa, where the NGACv2 results are close to the MERRA-2 reanalysis, with over prediction in August 2019 and low biases from December 2019 to March 2020. In addition to its general under prediction of MERRA-2 total AOD, NGACv2 is not able to capture the temporal variations of total AOD in some regions, such as the enhanced AOD due to fire emissions in Southern Africa, South Atlantic and South America. Though NGACv2 shows similar temporal variations to MERRA-2 total AOD in Europe, East Asia, and the US, the magnitudes of NGACv2 predictions are too low by a factor of 1 to 3. This analysis is consistent with a 1-year evaluation of GEFS-Aerosols AOD that shows improvements over NGACv2 [Bhattacharjee et al., 2021]

5. ATom-1 retrospective forecast evaluation

Retrospective simulations of GEFS-Aerosols and NGACv2 were performed for the summer of 2016 and evaluated using aircraft measurements from the first deployment of the Atmospheric Tomography Mission (ATom-1) in July and August 2021. During ATom-1, plumes from dust storms and large biomass burning events and low-level sea salt aerosols were observed over the southern and central Atlantic, and anthropogenic pollution was observed over the United States on the last flight from Minnesota to Southern California.

In this section, we evaluate the 24-hour forecast skill of GEFS-Aerosols and NGACv2 by comparing with ATom-1 observations. The GEFS-Aerosols and NGACv2 model results are sampled at the same latitude, longitude and altitude as the ATom-1 measurements. The model output is hourly with ~25km horizontal resolution on the FV3 native grid. The ATom-1 measurements collected on a 1-second time base were compared to the nearest hour's model forecast. Model data is interpolated vertically (according to log-Z above ground level), but sampled within the nearest horizontal grid as the observations (with no horizontal interpolation). Thus, the inherent differences between temporal (differences of up to 0.5 hour) and spatial scales of the observations (~200 m resolution) and model results (25-100 km resolution) must be kept in mind with the model-measurement comparisons.

5.1 Global flight track column sum comparisons

Figure 14 shows the tropospheric column sums of OC along the flight tracks of the NASA DC-8 for the ATom-1 observations and GEFS-Aerosols model experiments. The OC column sums using GBBEPx V3 fire emissions at ~25 km resolution (Fig. 14 (b) are quite consistent and comparable to the observations. The modeled OC column sums are somewhat smaller than those of observation over the north Atlantic, Greenland, and southeastern Canada.

Results of the model-measurement comparisons for dust are shown in Figure 15. GEFS-Aerosols simulations show good agreement with ATom-1 observations over tropical north Atlantic and downwind of the western Africa dust source region. However, the model overestimates the dust columns over tropical south Atlantic, Greenland, southeastern Canada, while underestimating dust over the US, Alaska and broad areas of the Pacific Ocean. The GEFS-Aerosols model shows a clear enhancement of the dust event sampled on 8/17/16 east of the African coastline near 22°N, though the model column maxima tend to be more than a factor of 5 lower that the observations.

Table 3 gives median bias and correlation statistics for column sums of all GEFS-Aerosols model cases as well as the NGAC dust forecasts for ~130 profiles illustrated in Figures 14 and 15. Correlations (r – Pearson correlation coefficients) are typically above 0.7 for all species except dust. The OC differences noted above for GBBEPx are apparent in the bias statistics of OC (a factor of 2.5) and BC (a factor of 50%), although R-correlations are not significantly affected. Differences in the fire inventories also affect sulfate biases slightly (12%). For all species except for dust, decreases in median model/observed ratios are seen for the model results.

Dust, on the other hand, shows a slight underprediction in column amount in the model results. Dust sources depend critically on surface wind speed, have very little overlap with the anthropogenic and biomass-burning sources of the other species, and are associated with areas of weather and surface conditions, all which may contribute to the different response of dust emissions. Correlations of dust are also much lower than for other species, and there is a very obviously difference between GEFS-Aerosols and NGAC model forecast statistics as discussed further below. We note that sea-salt columns are not calculated or compared to ATom-1 observations, due to the large amount of observations below the detection limit, especially above 2 km altitude.

5.2 Vertical profile statistics comparisons

ATom-1 flight tracks are separated into 2 sections and labeled as the "Pacific" side for July 29 to August 8 2016 flights and the "Atlantic" side for August 15 to August 23 2016 flights. For this analysis the 1-second model and observed data are binned into 10 equally spaced vertical intervals (~1km) covering the vertical extent of the ATom-1 profiles. Figure 16 shows median, ratio and correlation statistics of OC, BC and sulfate for the 2 geographic regions and the two model cases. For OC over the Pacific, the median values are lower than that of the observation by more than 50%. Their correlations with observation are quite similar above ~3 km height. The vertical profile of ratio also suggests that the OC concentrations are underpredicted over Pacific. Statistics for the Atlantic flight tracks of ATom-1 show similar trends and behavior. The median values of model prediction OC are quite comparable to observations, which show very consistent vertical variation similar to the observations. The correlations with observations improve below 4 km height compared to those of the Pacific with the maximum closed to 0.80. While the correlations decrease significantly at 3-6 km height, it increases almost 50% above 6km height. The model results are biased too low below ~3km. The BC vertical profile statistics are quite different to OC with the model forecasts much larger than observations as one goes higher in altitude over both the Pacific and Atlantic section. Correlation coefficients with observations are about 0.6-0.8 from near surface to ~ 6km over Pacific and about 0.7-0.9 below ~4km over Atlantic. The correlations of both OC and BC decrease significantly above ~4km over the Atlantic. For sulfate, the median biases of model are biased too low from near surface to ~ 8 km over the Pacific and their correlation coefficients with observations are about 0.4-0.6 below 6 km. For the Atlantic, median values are quite comparable to the observation below ~7 km and their correlations are about 0.3~0.9 and consistently decreasing with altitude. By contrast, the Pacific comparisons for sulfate show a significant underprediction (60-70%) from the 0.5 to 7.0 km altitude for both model cases, which suggests a significant underprediction of oceanic gas-phase sulfur sources, such as DMS.

Vertically resolved statistics of naturally occurring dust and sea salt are shown in Figure 17. For dust over the Pacific, median values of GEFS-Aerosols are too low while the NGACv2 results are too high compared with the observations, and the correlations are almost less than 0.5. The performance of GEFS-Aerosols improves over the Atlantic with median values comparable to observations above ~4km and the correlation coefficients increasing to 0.5~0.8 below ~5km. While it is still showing a significant high bias for the NGACv2 model over Atlantic. For sea salt, the median values biases are all biased too low over both the Pacific and Atlantic. Generally, the correlations are much better below ~6 km.

5.3 Height-latitude profile comparisons over the Atlantic during ATom-1

The ATom-1 flight profiles allow a more detailed comparison of aerosol spatial patterns from different aerosol sources with the model. High values of OC and BC from fires were observed on 8/15/16 and 8/17/16 over the Atlantic, as were high values of dust and sea-salt. The flight track of height-latitude profiles of OC, BC and sulfate for these combined days are shown in Figure 18 for the ATom-1 measurements and the model results. The model results show similar pattern as the ATOM-1 in reproducing the profiles of OC even using log scale, especially the biomass burning plumes near the tropics, though the model

results show slightly low biases. But they also show some bias for OC at levels above 4~5 km over the north Atlantic, where model results show high biases. Overall, predicted BC (middle column of Figure 18) is able to capture the decreasing trend with increasing altitude in the latitude-height profiles, however they are underpredicted in the biomass burning plumes near the tropics from the surface to 5 km height in both model experiments, which have been seen in other models due to insufficient wet scavenging [Wang et al., 2014, Choi et al., 2020]. Similar to the OC profiles, the model results overpredict above 4-5 km height levels. It appears the model does not reproduce the enhancements of BC at 1-4 km height very well over this area. It may be possibly due to relative weak convection or a low modeled injection height that the fire emission has not been lifted enough to this altitude, which need further studies. For sulfate (right column), the model experiments show high concentrations at low altitude, similar to the observations, though there are still some differences for the plume location at 2-4 km height that shift the plume from near the equator to near 20°N in the model experiments. Over the equatorial areas at about 2-4 km height, the observed sulfate concentration is underestimated by about 30% by modeled results, which may also relate to the injection height of biomass burning those results in much lower SO_2 at this altitude since SO_2 is one of the important precursors for sulfate production. Meanwhile, the sulfate concentration above 6 km is overestimated over the tropics while underestimated near the surface.

Figure 19 shows the comparisons of the naturally occurring dust and sea salt aerosols for the same time period. In the left column of dust, we also include the NGACv2 results. For more consistent comparisons, here the modeled dust results are summed up by the first two bins to match the observation particle size range (less than 3 μm). The GEFS-Aerosol predictions show agreement in the dust height-latitude profiles with the observations and exhibit similar patterns. The observed dust plumes are reproduced by the model over 15-35°N, but the model appears to underestimate wet removal in the upper levels that results in the overestimation of dust above 7-8 km height in northern Atlantic and above 5 km height in the tropical southern Atlantic. On the other hand, the NGACv2 prediction shows a very large bias over broad areas of the north Atlantic and the tropical southern Atlantic. A high dust plume near 35°S has not been captured well by the model from the surface to the upper levels, which may be caused by missing dust events over South America. For sea salt, the model results are able to predict patterns consistent with the observation, especially from the surface to about 4-6 km height.

6. Summary and future plan

Since the dynamical core of FV3 developed by GFDL has been selected by NOAA to be the dynamical core for the Next Generation Global Prediction System (NGGPS), development of a coupled weather and atmospheric chemical composition model for chemical weather and air quality forecasting based on the FV3 framework has begun couple of years ago. The development as a single ensemble member of the Global Ensemble Forecast System (GEFS) has been completed. This new model, referred to as GEFS-Aerosols, was implemented as one member of the GEFS into operations as part of NOAA's first coupled UFS model in September 2020 and replaced previous operational global aerosol prediction system NGACv2 at NCEP.

The chemical component of atmospheric composition in GEFS-Aerosols is based on WRF-Chem, which is a community modeling system used by thousands of users worldwide. The aerosol modules are based on modules from the GOCART model. Features of the new model include: 1) the biomass burning plume rise module added from WRF-Chem; 2) the FENGSHA dust scheme implemented and developed by NOAA Air Resources Laboratory (ARL); 3) all sub-grid scale tracer transport and deposition is handled inside the physics routines requiring consistent implementation of positive definite tracer transport and wet scavenging in the SAS scheme; 4) the updated background fields of OH, H_2O_2 and NO_3 from GMI model; 5) biomass-burning emission calculations based on the GBBEPx V3 emission and FRP provided by NESDIS; and 6） global anthropogenic emission inventories derived from CEDS and HTAP. This new model is able to forecast the higher-resolution distribution of primary air pollutants of aerosols: black carbon, organic carbon, sulfate, and dust and sea salt each with five size bins. Meanwhile, it is also capable of handling volcanic eruptions, which can inject vast quantities of particulates into the atmosphere. While for the predicted results in the paper, we have not included the volcanic emission into the model for the June 2019 Raikoke eruption, it may partially impact on the underprediction over high northern latitude.

Several sensitivity experiments using different emissions inputs indicate that the model shows the best performance matching the observations when configured to use the CEDS anthropogenic emission and GBBEPx V3 fire emissions with plume-rise module. For more extensive evaluation, we performed 9 months of Day-1 real-time forecast of GEFS-Aerosols starting in July 2019 and the predicted AOD was used to compare with the satellite observations from MODIS and VIIRS, reanalysis data of ICAP-MME and MERRA-2, AERONET observations, and the model predictions from MERRA-2 and NGACv2. Overall, GEFS-Aerosols is a substantial improvement for both composition and variability of aerosol distributions over those from the currently operational global aerosol prediction system of NGACv2. Globally, the GEFS-Aerosols predicted biases with respect to MERRA-2 forecast for dust, OC and sulfate AOD were improved compared to those from NGACv2. Substantial improvements were seen for the total AOD prediction when compared with MERRA-2 reanalysis during the period of July to November 2019. Though there are still some high biases over southern African fire region and eastern Asia and low biases over south America and dust source regions, GEFS-Aerosols reproduces the prominent temporal and geographical features of AOD as represented by satellite observations and reanalysis data, like dust plumes over North Africa and the Arabian Peninsula, biomass burning plumes in Southern Hemisphere, South America, Northwestern America and Eastern Europe, polluted air over Eastern and Southern Asia, and high-altitude sea-salt bands. We also sampled the forecast total AOD of GEFS-Aerosols and NGACv2 in the same location as 60 AERONET sites, which are spread globally and represent different aerosol regimes, and compared their variations for the 7/5/19-11/30/19. Much higher correlation coefficients against AERONET data are indicated for the GEFS-Aerosols than those for NGACv2 globally, and are quite comparable to those of the ICAP-MME.

During the biomass burning events, GEFS-Aerosols captured major fires over southern Africa, Siberia, Central Amazon and Central South America much better than NGACv2. Part of the improvement may be due to the vertical transport by the plume-rise module. Generally, the total AOD time series of GEFS-Aerosols predictions matches closely to those of ICAP and AERONET during most of the time from July to November 2019 at the AERONET sites over South America, except there

are some minor under predictions of several highest AOD episodes. In contrast, NGACv2 substantially underpredicted almost throughout the whole period and almost entirely missed many high AOD events. For the southern African event, the GEFS-Aerosols predictions are able to capture the daily total AOD variations seen in the AERONET observations, even better than that of the ICAP total AOD at the sites near the fire source regions, though there are overpredictions at the sites in downwind areas, which may be due to the lack of removal process or uncertainties of fire emission in central and southern Africa. In contrast, the NGACv2 results show under prediction in total AOD forecast at most of the AERONET sites in this region. Overall, the model predicts total AOD variation by GEFS-Aerosols indicates much better performance than that of NGACv2 over western North Africa. Although GEFS-Aerosols shows reductions in dust emissions over the Saharan dust source, the correlations with observations from downwind AERONET sites in western Africa are improved over those for NGACv2. The largest biases and discrepancies of GEFS-Aerosols and NGACv2 are both indicated in the sites in Tajikistan, which may be associated with a missing dust source near this site for both models.

We also evaluated predicted aerosols concentrations with different resolution against the ATom-1 aircraft measurements from July to August 2016. Overall, predicted aerosol concentrations are quite comparable to the ATom-1 measurements along the flight tracks globally with ~25 km model resolution. The model shows good performance in reproducing vertical profiles of OC, BC and sulfate, and the location of fire plumes was captured well overall. Sulfate over the Pacific, southern and tropical Atlantic is significantly underpredicted, suggesting an underestimation in the oceanic sulfur sources, such as DMS. A clear trend in increased overprediction with altitude for BC suggests that further refinements in characterizing precipitation scavenging of aerosol in GEFS-Aerosols is needed, since this is the only loss process for BC other than surface deposition.

This paper overviews advances and challenges in model development for operational atmospheric aerosol predictions at NOAA. This implementation advanced the global aerosol forecast capability for NOAA and made a step forward toward developing a global aerosol data assimilation system. Currently, the assimilation of AOD based on satellite observations is under development to constrain aerosol distributions in the GEFS-Aerosols model. Initial testing shows promise for improvement of predictions as well as limitations indicating the need for refinements in quality control, data assimilation impacts on aerosol composition and vertical distribution, as well as a need for bias correction of satellite observations. With bias and other errors substantially reduced in the GEFS-Aerosols, especially when it is equipped with an aerosol data assimilation system. Current, though the aerosol feedback from the aerosol components has not yet been included into the atmospheric model for direct and indirect radiative feedback, the model provides a good starting point from which to investigate at the impact on weather predictions out to sub-seasonal and seasonal scales when including the aerosol feedbacks on atmospheric system in the future plan.

Code and data availability

The GEFS-Aerosols v1 code and model configuration for aerosol forecast here are available at https://doi.org/10.5281/zenodo.5655290. ATom-1 data is publicly available at the Oak Ridge National Laboratory Distributed Active Archive Center: https://daac.ornl.gov/ATOM/guides/ATom_merge.html (Wofsy et al., 2018).

Author contribution

Li Zhang and Raffaele Montuoro were the major developers of the GEFS-Aerosols model, including implementing and coupling the aerosol components to the FV3GFSv15 meteorological model. Stuart McKeen helped to process the anthropogenic emission and background input data, provided suggestions during the development of GEFS-Aerosols, and evaluated the model performance with ATom-1 observations. Barry Baker developed and implemented the FENGSHA dust scheme into GEFS-Aerosols. Partha Bhattacharjee helped to evaluate the GEFS-Aerosols real-time and operational predictions. Georg Grell provided oversight of the model development. Li Zhang and Judy Henderson developed the workflow for GEFS-Aerosols prediction and worked with Li Pan to perform and manage the real-time and retrospective forecasts. R. Ahmadov provided guidance on the implementation of the fire plume rise scheme. Shobha Kondragunta, Xiaoyang Zhang, and Fangjun Li provided the GBBEPx V3 data. The other co-authors provided help, suggestions and project management throughout the GEFS-Aerosols modeling system development. Li Zhang prepared the manuscript with contributions from all co-authors.

Competing interests

The authors declare that they have no conflict of interest.

Acknowledgements

Li Zhang, Raffaele Montuoro, Haiqin Li and Ravan Ahmadov were supported by funding from NOAA GSL Award Number NA17OAR4320101. This work was also supported by the UFS Research to Operations Medium Range Weather/Seasonal to Subseasonal Atmospheric Composition sub-project.

Reference

Ahmadov R, Grell G, James E, Csiszar I, Tsidulko M, Pierce B, et al. Using VIIRS Fire Radiative Power data to simulate biomass burning emissions, plume rise and smoke transport in a real-time air quality modeling system. 2017 Ieee International Geoscience and Remote Sensing Symposium. IEEE International Symposium on Geoscience and Remote Sensing IGARSS. New York: Ieee; p. 2806-8, 2017.

Bauer, S. E., Im, U., Mezuman, K., & Gao, C. Y.: Desert dust, industrialization, and agricultural fires: Health impacts of outdoor air pollution in Africa. Journal of Geophysical Research: Atmospheres, 124, 4104– 4120. https://doi.org/10.1029/2018JD029336, 2019.

Bhattacharjee, P. S., Wang, J., Lu, C.-H., and Tallapragada, V.: The implementation of NEMS GFS Aerosol Component (NGAC) Version 2.0 for global multispecies forecasting at NOAA/NCEP – Part 2: Evaluation of aerosol optical thickness, Geosci. Model Dev., 11, 2333–2351, https://doi.org/10.5194/gmd-11-2333-2018, 2018.

Bhattacharjee, P. S., Zhang, L., Baker, B., Pan, L., Montuoro, R., Grell A. G., and McQueen, J. Evaluation of Aerosol Optical Depth forecast from NOAA's Global Aerosol Forecast Model (GEFS-Aerosols). To be submitted. 2021.

Black, T. L., Abeles, J. A., Blake, B. T., Jovic, D., Rogers, E., Zhang, X., Aligo, E. A. , Dawson, L. C. , Lin, Y., Strobach, E. , Shafran, P. C., Carley, J. R.. A limited area modeling capability for the Finite-Volume Cubed-Sphere (FV3) dynamical core and comparison with a global two-way nest. Journal of Advances in Modeling Earth Systems, 13, e2021MS002483. https://doi.org/10.1029/2021MS002483, 2021.

Bourgeois, I., Peischl, J., Thompson, C. R., Aikin, K. C., Campos, T., Clark, H., Commane, R., Daube, B., Diskin, G. W., Elkins, J. W., Gao, R.-S., Gaudel, A., Hintsa, E. J., Johnson, B. J., Kivi, R., McKain, K., Moore, F. L., Parrish, D. D., Querel, R., Ray, E., Sánchez, R., Sweeney, C., Tarasick, D. W., Thompson, A. M., Thouret, V., Witte, J. C., Wofsy, S. C., and Ryerson, T. B.: Global-scale distribution of ozone in the remote troposphere from the ATom and HIPPO airborne field missions, Atmos. Chem. Phys., 20, 10611–10635, https://doi.org/10.5194/acp-20-10611-2020, 2020.

Bozzo, A., Benedetti, A., Flemming, J., Kipling, Z., and Rémy, S.: An aerosol climatology for global models based on the tropospheric aerosol scheme in the Integrated Forecasting System of ECMWF, Geosci. Model Dev., 13, 1007–1034, https://doi.org/10.5194/gmd-13-1007-2020, 2020.

Burnett, R., Chen, H., Szyszkowicz, M., Fann, N., Hubbell, B., Pope, C. A., Spte, J.S., Brauer, M., Cohen, A., Weichenthal, S., Coggins, J., Di, Q., Brunekreef, B., Frostad, F., Lim, S.S., Kan, H., Walker, K.d., Thurston, G.D., Hayes, R.b., Lim, C.C., Turner, M. C., Jerrett, M., Krewski, D., Gapstur, S.M., Diver, W.R., Ostro, B., Goldberg, D., Crouse, D.L., Martin, R.V., Peters, P., Pinault, L., Tjepkema, M., Donkelaar, A., Villeneuve, P.J., Miller, A.B., Yin, P., Zhou, M., Wang, L., Janssen N.A.H., Marra, M., Atkinson, R.W., Tsang, H., Thach, T.Q., Cannon, J.B., Allen, R.T., Hart, J.E., Laden, F., Cesaroni, G., Forastisere, F., Weinmayr, G., Jaensch, A., Nagel, G., Concin, H., and Spadaro, J.V.: Global estimates of mortality associated with longterm exposure to outdoor fine particulate matter, P. Natl. Acad. Sci. USA, 115(38), 9592–9597, doi:10.1073/pnas.1803222115, 2018.

Chappell, A., and Webb, N. P.: Using albedo to reform wind erosion modelling, mapping and monitoring. Aeolian Research, 23, 63–78. https://doi.org/10.1016/j.aeolia.2016.09.006, 2016.

Chen, J. M., Li, C. L., Ristovski, Z., Milic, A., Gu, Y. T., Islam, M. S., Wang, S. X., Hao, J. M., Zhang, H. F., He, C. R., Guo, H., Fu, H. B., Miljevic, B., Morawska, L., Thai, P., Fat, L., Pereira, G., Ding, A. J., Huang, X., and Dumka, U. C.: A review of biomass burning: Emissions and impacts on air quality, health and climate in China, Sci. Total Environ., 579, 1000–1034, https://doi.org/10.1016/j.scitotenv.2016.11.025, 2017.

Chen, Q., Yin, Y., Jin, L.-J., Xiao, H., Zhu, S.-Ch.: The effect of aerosol layers on convective cloud microphysics and precipitation, Atmos. Res., 101 (1-2), pp. 327–340 http://doi.org/10.1016/j.atmosres.2011.03.007, 2011.

Chin, M., Rood, B. R., Lin, S.-J., Muller, F. J., and Thomspon, M. A.: Atmospheric sulfur cycle in the global model GOCART: Model description and global properties, J. Geophys. Res., 105, 24,671-24,687, 2000.

Chin, M., Ginoux, P., Kinne, S., Torres, O., Holben, B., Duncan, B., Martin, R., Logan, J., Higurashi, A., and Nakajima, T.: Tropospheric aerosol optical thickness from the GOCART model and comparisons with satellite and Sun photometer measurements, J. Atmos. Sci., 59, 461–483, 2002.

Choi, Y., Kanaya, Y., Takigawa, M., Zhu, C., Park, S.-M., Matsuki, A., Sadanaga, Y., Kim, S.-W., Pan, X., and Pisso, I.: Investigation of the wet removal rate of black carbon in East Asia: validation of a below- and in-cloud wet removal scheme in

FLEXible PARTicle (FLEXPART) model v10.4, Atmos. Chem. Phys., 20, 13655–13670, https://doi.org/10.5194/acp-20-13655-2020, 2020.

Colarco, P. R., Kahn, R. A., Remer, L. A., and Levy, R. C.: Impact of satellite viewing-swath width on global and regional aerosol optical thickness statistics and trends, Atmos. Meas. Tech., 7, 2313–2335, https://doi.org/10.5194/amt-7-2313-2014, 2014.

Colarco, P., da Silva, A., Chin, M., and Diehl, T.: Online simulations of global aerosol distributions in the NASA GEOS-4 model and comparisons to satellite and ground-based aerosol optical depth, J. Geophys. Res., 115, D14207, doi:10.1029/2009JD012820, 2010.

Darmenov, A. and da Silva, A.: The Quick Fire Emissions Dataset (QFED) – Documentation of versions 2.1, 2.2 and 2.4, NASA Technical Report Series on Global Modeling and Data As- similation, NASA/TM-2015–104606, Vol. 38, 211 pp., avail- able at: http://citeseerx.ist.psu.edu/viewdoc/download?doi=10.1. 1.406.7724&rep=rep1&type=pdf (last access: 4 June 2018), 2015.

Diehl, T., Heil, A., Chin, M., Pan, X., Streets, D., Schultz, M., and Kinne, S.: Anthropogenic, biomass burning, and volcanic emis- sions of black carbon, organic carbon, and SO2 from 1980 to 2010 for hindcast model experiments, Atmos. Chem. Phys. Dis- cuss., 12, 24895–24954, https://doi.org/10.5194/acpd-12-24895-2012, 2012.

Easter, R. C., Ghan, S. J., Zhang, Y., Saylor, R. D., Chapman, E. G., Laulainen, N. S., Abdul-Razzak, H., Leung, L. R., Bian, X., and Zaveri, R. A.: MIRAGE: Model Description and Evaluation of Aerosols and Trace Gases. J. Geophys. Res., 109, D20210, doi:10.1029/2004JD004571, 2004.

Eck, T. F., Holben, B. N., Reid, J. S., Dubovik, O., Smirnov, A., O'Neill, N. T., Slutsker, I., and Kinne, S.: The wavelength dependence of the optical depth of biomass burning, urban and desert dust aerosols, J. Geophys. Res., 104, 31333–31350, 1999.

Fast, J. D., Gustafson Jr., I. W., Easter, C. R., Zaveri, A. R., Barnard, C. J., Chapman, G. E., Grell, A. G., and Peckham, E. S.: Evolution of ozone, particulates, and aerosol direct radiative forcing in the vicinity of Houston using a fully coupled meteorology-chemistry-aerosol model. J. Geophys. Res., 111, D21305, doi:10.1029/2005JD006721, 2006.

Fécan, F., Marticorena, B. and Bergametti, G.: Parametrization of the increase of the aeolian erosion threshold wind friction velocity due to soil moisture for arid and semi-arid areas. Annales Geophysicae 17, 149–157, https://doi.org/10.1007/s00585-999-0149-7, 1998.

Forkel, R., Werhahn, J., Buus Hansen, A., McKeen, S., Peckham, S., Grell, G., Suppan, P.: Effect of aerosol-radiation feedback on regional air qualityeacase study with WFR/Chem. Atmos. Environ. 53, 202e211.http://dx.doi.org/10.1016/j.atmosenv.2011.10.009, 2012

Freitas, S. R., Longo, K. M., Alonso, M. F., Pirre, M., Marecal, V., Grell, G., Stockler, R., Mello, R. F., and Sánchez Gácita, M.: PREP-CHEM-SRC – 1.0: a preprocessor of trace gas and aerosol emission fields for regional and global atmospheric chemistry models, Geosci. Model Dev., 4, 419-433, doi:10.5194/gmd-4-419-2011, 2011.

Freitas, S. R., Longo, K. M., Chatfield, R., Latham, D., Silva Dias, M. A. F., Andreae, M. O., Prins, E., Santos, J. C., Gielow, R., and Carvalho Jr., J. A.: Including the sub-grid scale plume rise of vegetation fires in low resolution atmospheric transport models, Atmos. Chem. Phys., 7, 3385–3398, https://doi.org/10.5194/acp-7-3385-2007, 2007.

Froyd, K. D., Murphy, D. M., Brock, C. A., Campuzano-Jost, P., Dibb, J. E., Jimenez, J.-L., Kupc, A., Middlebrook, A. M., Schill, G. P., Thornhill, K. L., Williamson, C. J., Wilson, J. C., and Ziemba, L. D.: A new method to quantify mineral dust and other aerosol species from aircraft platforms using single-particle mass spectrometry, Atmos. Meas. Tech., 12, 6209–6239, https://doi.org/10.5194/amt-12-6209-2019, 2019.

Gelaro, R., McCarty, W., Suárez, M. J., Todling, R., Molod, A., Takacs, L., Randles, C. A., Darmenov, A., Bosilovich, M. G., Reichle, R., Wargan, K., Coy, L., Cullather, R., Draper, C., Akella, S., Buchard, V., Conaty, A., da Silva, A. M., Gu, W., Kim, G., Koster, R., Lucchesi, D. Merkova, J. E., Nielsen, G. Partyka, G., Pawson, S., Putman, W., Rienecker, M., Schubert, S. D.,

Sienkiewicz, M., and Zhao, B.: The Modern-Era Retrospective Analysis for Research and Applications, Version 2 (MERRA-2), J. Climate, 30, 5419–5454, https://doi.org/10.1175/JCLI-D-16-0758.1, 2017.

Gillette, D. A., Adams, J., Endo, A., Smith, D., and Kihl, R.: Threshold velocities for input of soil particles into the air by desert soils, J. Geophys. Res., 85(C10), 5621– 5630, doi:10.1029/JC085iC10p05621, 1980.

Gillette, D. A.: Threshold friction velocities for dust production for agricultural soils. Journal of Geophysical Research, 93(D10), 12645–12662. https://doi.org/10.1029/jd093id10p12645, 1988.

Grell, G. A., Peckham, E. S., Schmitz, R., McKeen, A. S., Frost, G., Skamarock, W., and Eder, B.: Fully-coupled online chemistry within the WRF model. Atmospheric Environment, 39, 6957-6975, doi:10.1016/j.atmosenv.2005.04.027, 2005.

Grell, G., Freitas, S. R., Stuefer, M., and Fast, J.: Inclusion of biomass burning in WRF-Chem: impact of wildfires on weather forecasts, Atmos. Chem. Phys., 11, 5289-5303, https://doi.org/10.5194/acp-11-5289-2011, 2011.

Haustein, K., Pérez, C., Baldasano, J. M., Jorba, O., Basart, S., Miller, R. L., Janjic, Z., Black, T., Nickovic, S., Todd, M. C., Washington, R., Müller, D., Tesche, M., Weinzierl, B., Esselborn, M., and Schladitz, A.: Atmospheric dust modeling from meso to global scales with the online NMMB/BSC-Dust model – Part 2: Experimental campaigns in Northern Africa, Atmos. Chem. Phys., 12, 2933-2958, https://doi.org/10.5194/acp-12-2933-2012, 2012.

Hoesly et al, Historical (1750–2014) anthropogenic emissions of reactive gases and aerosols from the Community Emissions Data System (CEDS). Geosci. Model Dev. 11, 369-408, 2018.

Holben, B. N., Eck, T. F., Slutsker, I., Tanré, D., Buis, J. P., Setzer, A., Vermote, E., Reagan, J. A., Kaufman, Y. J., Nakajima, T., Lavenu, F., Jankowiak, I., and Smirnov, A.: AERONET – A Federated instrument network and data archive for aerosol characterization, Remote Sens. Environ., 66, 1–16, 1998.

Hsu, N. C., Jeong, M.-J., Bettenhausen, C., Sayer, A. M., Hansell, R., Seftor, C. S., Huang, J., and Tsay, S.-C.: Enhanced Deep Blue aerosol retrieval algorithm: The second generation, J. Geophys. Res.-Atmos., 118, 9296–9315, https://doi.org/10.1002/jgrd.50712, 2013.

Jackson, J., Liu, H., Laszlo, I., Kondragunta, S., Remer, L. A., Huang, J., and Huang, H.-C.: Suomi-NPP VIIRS Aerosol Algorithms and Data Products, J. Geophys. Res., 118, 12673–12689, https://doi.org/10.1002/2013jd020449, 2013.

Janssens-Maenhout, G., Crippa, M., Guizzardi, D., Dentener, F., Muntean, M., Pouliot, G., Keating, T., Zhang, Q., Kurokawa, J., Wankmüller, R., Denier van der Gon, H., Kuenen, J. J. P., Klimont, Z., Frost, G., Darras, S., Koffi, B., and Li, M.: HTAP_v2.2: a mosaic of regional and global emission grid maps for 2008 and 2010 to study hemispheric transport of air pollution, Atmos. Chem. Phys., 15, 11411-11432, https://doi.org/10.5194/acp-15-11411-2015, 2015.

Janssens-Maenhout, G.: EDGARv4.1 Emission Time Series, European Commission, Joint Research Centre (JRC) [Dataset] PID, available at: http://data.europa.eu/89h/jrc-edgar-emissiontimeseriesv41 (last access: 12 June 2018), 2010.

Levin, Z., and Cotton R. W.: Aerosol Pollution Impact on Precipitation, Aerosol Pollution Impact on Precipitation: A Scientific Review, 407 pp., Springer, New York, 2009.

Levy, R. C., Mattoo, S., Munchak, L. A., Remer, L. A., Sayer, A. M., Patadia, F., and Hsu, N. C.: The Collection 6 MODIS aerosol products over land and ocean, Atmos. Meas. Tech., 6, 2989–3034, https://doi.org/10.5194/amt-6-2989-2013, 2013.

Liu, F., Zhang, Q., van der A, R. J., Zheng, B., Tong, D., Yan, L., Zheng, Y., and He, K.: Recent reduction in NOx emissions over China: synthesis of satellite observations and emission inventories, Environ. Res. Lett., 11, 114002, https://doi.org/10.1088/1748-9326/11/11/114002, 2016.

Liu, H., Remer, L. A., Huang, J., Huang, H.-C., Kondragunta, S., Laszlo, I., Oo, M., and Jackson, J. M.: Preliminary Evaluation of Suomi-NPP VIIRS Aerosol Optical Thickness, J. Geophys. Res., 119, 3942–3962, https://doi.org/10.1002/2013jd020360, 2013.

Lu, C.-H., da Silva, A.,Wang, J., Moorthi, S., Chin, M., Colarco, P., Tang, Y., Bhattacharjee, P. S., Chen, S.-P., Chuang, H.-Y., Juang, H.-M. H., McQueen, J., and Iredell, M.: The implementation of NEMS GFS Aerosol Component (NGAC) Version

1.0 for global dust forecasting at NOAA/NCEP, Geosci. Model Dev., 9, 1905–1919, https://doi.org/10.5194/gmd-9-1905-2016, 2016.

Lu, S., Huang, H.-C., Hou, Y.-T., Tang, Y., McQueen, J., da Silva, A., Chin, M., Joseph, E., and Stockwell, W.: Development of NCEP Global Aerosol Forecasting System: an overview and its application for improving weather and air quality forecasts, in: NATO Science for Peace and Security Series: Air Pollution Modelling and Its Application XX, Springer Publications, Dordrecht, the Netherlands, 451–454, https://doi.org/10.1007/978-90-481-3812-8, 2010.

MacKinnon, D. J., Clow, G. D., Tigges, R. K., Reynolds, R. L., and Chaves Jr. P. S.: Comparison of aerodynamically and model-derived roughness lengths (z0) over diverse surfaces, central Mojave Desert, California, USA, Geomorphology, 63, 103– 113, doi:10.1016/j.geomorph.2004.03.009, 2004

Marticorena, B. and Bergametti, G.: Modeling the atmospheric dust cycle: 1-Design of a soil derived dust production scheme, J. Geophys. Res., 100, 16415-16430, 1995.

Muhlbauer, A., Grabowski, W. W., Malinowski, P. S., Ackerman, P. T., Bryan, H. G., Lebo, J. Z., Milbrandt, A. J., Morrison, H., Ovchinnikov, M., Tessendorf, S., Thériault, G. J.M.: Thompson Reexamination of the state of the art of cloud modelling shows real improvements, Bull. Am. Meteorol. Soc., 94, pp. ES45–ES48 http://doi.org/10.1175/BAMS-D-12-00188.1, 2013.

Mulcahy, J. P., Walters, D. N., Bellouin, N., and Milton, S. F.: Impacts of increasing the aerosol complexity in the Met Office global numerical weather prediction model, Atmos. Chem. Phys., 14, 4749-4778, doi:10.5194/acp-14-4749-2014, 2014.

Murphy, D. M., Froyd, K. D., Bian, H., Brock, C. A., Dibb, J. E., DiGangi, J. P., Diskin, G., Dollner, M., Kupc, A., Scheuer, E. M., Schill, G. P., Weinzierl, B., Williamson, C. J., and Yu, P.: The distribution of sea-salt aerosol in the global troposphere, Atmos. Chem. Phys., 19, 4093–4104, https://doi.org/10.5194/acp-19-4093-2019, 2019.

Murphy, D., Froyd, K., Apel, E.,Blake, R. D., Blake, J. N., Evangeliou, N., Hornbrook, S. R., Peischl, J., Ray, E., Ryerson,B. T., Thompson, C., and Stohl, A.: An aerosol particle containing enriched uranium encountered in the remote T upper troposphere, J. Environ. Radioactivity, 184–185, 95-100, doi:10.1016/j.jenvrad.2018.01.006, 2018

Owen, P. R.: Saltation of uniform grains in air. Journal of Fluid Mechanics, 20(2), 225–242. https://doi.org/10.1017/S0022112064001173, 1964.

Powers, J. G., Klemp, J. B., Skamarock, W. C., Davis, C. A., Dudhia, J., Gill, D. O., Coen, J. L., Gochis, D. J., Ahmadov, R., Peckham, S. E., Grell, G. A., Michalakes, J., Trahan, S., Benjamin, S. G., Alexander, C. R., Dimego, G. J., Wang, W., Schwartz, C. S., Romine, G. S., Liu, Z., Snyder, C., Chen, F., Barlage, M. J., Yu, W., & Duda, M. G. : The Weather Research and Forecasting Model: Overview, System Efforts, and Future Directions, Bulletin of the American Meteorological Society, 98(8), 1717-1737, 2017.

Prigent, C., Jiménez, C., and Catherinot, J.: Comparison of satellite microwave backscattering (ASCAT) and visible/near-infrared reflectances (PARASOL) for the estimation of aeolian aerodynamic roughness length in arid and semi-arid regions, Atmos. Meas. Tech., 5, 2703–2712, https://doi.org/10.5194/amt-5-2703-2012, 2012.

Raupach, M. R.: Drag and drag partition on rough surfaces. Boundary-Layer Meteorology. https://doi.org/10.1007/BF00155203, 1992.

Reale, O., Lau, K. M., and Silva da, A.: Impact of interactive aerosol on the African easterly jet in the NASA GEOS-5 Global Forecasting System. Wea. Forecasting, 26, 504–519, 2011.

Reid, J., Benedetti, A., Colarco, P. R., and Hansen, J. A.: International operational aerosol observability work-shop, B. Am. Meteorol. Soc., 92, ES21-ES24, https://doi.org/10.1175/2010BAMS3183.1, 2011.

Rodwell, M. J. and Jung, T.: Understanding the local and global impacts of model physics changes: an aerosol example, Q.J.R. Meteorol. Soc., 134, 1479–1497, doi:10.1002/qj.298, 2008.

Rosenfeld, D., Woodley, W. L., Khain, A., Cotton, W. R., Carrió, G., Ginis, I., and Golden, J. H.: Aerosol effects on microstructure and intensity of the tropical cyclones, B. Am. Meteorol. Soc. 93, 987–1001, 2012.

Sayer, A. M., Hsu, N. C., Bettenhausen, C., and Jeong, M.-J.: Validation and uncertainty estimates for MODIS Collection 6 "Deep Blue" aerosol data, J. Geophys. Res.-Atmos., 118, 7864–7872, https://doi.org/10.1002/jgrd.50600, 2013.

Sayer, A. M., Munchak, L. A., Hsu, N. C., Levy, R. C., Bettenhausen, C., and Jeong M.-J.: MODIS Collection 6 aerosol products: Comparison between Aqua's e-Deep blue, dark target and "merged" data sets and usage recommendations, J. Geophys. Res.-Atmos., 119, 13965–989, 2014.

Schill, G.P., Froyd, K.D., Bian, H. et al. Widespread biomass burning smoke throughout the remote troposphere. Nat. Geosci. 13, 422–4. https://doi.org/10.1038/s41561-020-0586-1, 2020

Sessions, W. R., Reid, J. S., Benedetti, A., Colarco, P. R., da Silva, A., Lu, S., Sekiyama, T., Tanaka, T. Y., Baldasano, J. M., Basart, S., Brooks, M. E., Eck, T. F., Iredell, M., Hansen, J. A., Jorba, O. C., Juang, H.-M. H., Lynch, P., Morcrette, J.-J., Moorthi, S., Mulcahy, J., Pradhan, Y., Razinger, M., Sampson, C. B., Wang, J., and Westphal, D. L.: Development towards a global operational aerosol consensus: basic climatological characteristics of the International Cooperative for Aerosol Prediction Multi-Model Ensemble (ICAP-MME), Atmos. Chem. Phys., 15, 335–362, https://doi.org/10.5194/acp-15-335-2015, 2015

Shao, Y., Raupach, M. R., and Findlater, P. A.: Effect of saltation bombardment on the entrainment of dust by wind. Journal of Geophysical Research, 98(D7), 12719–12726. https://doi.org/10.1029/93jd00396, 1993.

Shao, Y., Ishizuka, M., Mikami, M., and Leys, J. F.: Parameterization of size-resolved dust emission and validation with measurements. Journal of Geophysical Research Atmospheres, 116(8), D08203. https://doi.org/10.1029/2010JD014527, 2011.

Shi, X., and Brasseur, G. P.: The response in air quality to the reduction of Chinese economic activities during the COVID-19 outbreak. Geophysical Research Letters, 47, e2020GL088070. https://doi.org/10.1029/2020GL088070, 2020.

Slinn, W. G. N.: Precipitation scavenging, in Atmospheric Science and Power Production, edited by: D. Randerson, U.S. Dept. of Energy, Washington D. C., 472–477, 1984.

Theurich, G., DeLuca, C., Campbell, T., Liu, F., Saint, K., Vertenstein, M., Chen, J., Oehmke, R., Doyle, J., Whitcomb, T., Wallcraft, A., Iredell, M., Black, T., da Silva, A.M., Clune, T., Ferraro, R., Li, P., Kelley, M., Aleinov, I., Balaji, V., Zadeh, N., Jacob, R., Kirtman, B., Giraldo, F., McCarren, D., Sandgathe, S., Peckham, S., and Dunlap, IV, R.: The Earth System Prediction Suite: Toward a coordinated U.S. modeling capability. Bull. Amer. Meteorol. Soc., 97, no. 7, 1229-1247, doi:10.1175/BAMS-D-14-00164.1, 2016.

Thomson, D.S., Schein, M. E., Murphy, D.M.: Particle analysis by laser mass spectrometry WB-57F instrument overview. Aero. Sci. Technol. 33, 153–169, 2000.

Tong, D. Q., Wang, J. X. L., Gill, T. E., Lei, H., and Wang, B.: Intensified dust storm activity and Valley fever infection in the southwestern United States, Geophys. Res. Lett., 44, 4304– 4312, doi:10.1002/2017GL073524, 2017.

Wang, H., Rasch, J. P., Easter, C. R., Singh, B., Zhang, R., Ma, P.-L., Qian, Y., Ghan, J. S., and Beagley, N.: Using an explicit emission tagging method in global modeling of source receptor relationships for black carbon in the Arctic: Variations, sources, and transport pathways, J. Geophys. Res. Atmos., 119, 12,888–12,909, doi:10.1002/2014JD022297, 2014.

Wang, J., Bhattacharjee, P. S., Tallapragada, V., Lu, C.-H., Kondragunta, S., da Silva, A., Zhang, X., Chen, S.-P., Wei, S.-W., Darmenov, A. S., McQueen, J., Lee, P., Koner, P., and Harris, A.: The implementation of NEMS GFS Aerosol Component (NGAC) Version 2.0 for global multispecies forecasting at NOAA/NCEP – Part 1: Model descriptions, Geosci. Model Dev., 11, 2315–2332, https://doi.org/10.5194/gmd-11-2315-2018, 2018.

Wang, Q., Jacob, J. D., Spackman, R. J., Perring, E. A., Schwarz, P. J., Moteki, N., Marais, A. E., Ge, C., Wang, J., and Barrett, R. H. S.: Global budget and radiative forcing of black carbon aerosol: Constraints from pole-to-pole (HIPPO) observations across the Pacific, J. Geophys. Res. Atmos., 119, 195–206, doi:10.1002/2013JD020824, 2014.

Wang Q, Su M.: A preliminary assessment of the impact of COVID-19 on environment–a case study of China. Sci Total Environ, 728:138915. doi: 10.1016/j.scitotenv.2020.138915, 2020.

Wofsy, S. C., Afshar, S., Allen, H. M., Apel, E., Asher, E. C., Barletta, B., Bent, J., Bian, H., Biggs, B. C., Blake, D. R., Blake, N., Bourgeois, I., Brock, C. A., Brune, W. H., Budney, J. W., Bui, T. P., Butler, A., Campuzano-Jost, P., Chang, C. S., Chin, M., Commane, R., Correa, G., Crounse, J. D., Cullis, P. D., Daube, B. C., Day, D. A., Dean-Day, J. M., Dibb, J. E., Di- Gangi, J. P., Diskin, G. S., Dollner, M., Elkins, J. W., Erdesz, F., Fiore, A. M., Flynn, C. M., Froyd, K., Gesler, D. W., Hall, S. R., Hanisco, T. F., Hannun, R. A., Hills, A. J., Hintsa, E. J., Hoffman, A., Hornbrook, R. S., Huey, L. G., Hughes, S., Jimenez, J. L., Johnson, B. J., Katich, J. M., Keeling, R. F., Kim, M. J., Kupc, A., Lait, L. R., Lamarque, J.-F., Liu, J., McKain, K., Mclaughlin, R. J., Meinardi, S., Miller, D. O., Montzka, S. A., Moore, F. L., Morgan, E. J., Murphy, D. M., Murray, L. T., Nault, B. A., Neuman, J. A., Newman, P. A., Nicely, J. M., Pan, X., Paplawsky, W., Peischl, J., Prather, M. J., Price, D. J., Ray, E., Reeves, J. M., Richardson, M., Rollins, A. W., Rosenlof, K. H., Ryerson, T. B., Scheuer, E., Schill, G. P., Schroder, J. C., Schwarz, J. P., St.Clair, J. M., Steenrod, S. D., Stephens, B. B., Strode, S. A., Sweeney, C., Tanner, D., Teng, A. P., Thames, A. B., Thompson, C. R., Ullmann, K., Veres, P. R., Vieznor, N., Wagner, N. L., Watt, A., Weber, R., Weinzierl, B., Wennberg, P., Williamson, C. J., Wilson, J. C., Wolfe, G. M., Woods, C. T., and Zeng, L. H.: ATom: Merged Atmospheric Chemistry, Trace Gases, and Aerosols, ORNL DAAC, Oak Ridge, Ten- nessee, https://doi.org/10.3334/ornldaac/1581, 2018.

Xian, P., Reid, J. S., Hyer, E. J. et al. Current state of the global operational aerosol multi-model ensemble: An update from the International Cooperative for Aerosol Prediction (ICAP). Q J R Meteorol Soc., 145 (Suppl. 1): 176– 209. https://doi.org/10.1002/qj.3497, 2019.

Xie, S. P., B. Lu, and Xiang, Q. B.: Similar spatial patterns of climate responses to aerosol and greenhouse gas changes. Nat. Geosci., 6, 828–832, doi:https://doi.org/10.1038/ngeo1931, 2013.

Xing, J., Li, S., Jiang, Y., Wang, S., Ding, D., Dong, Z., Zhu, Y., and Hao, J.: Quantifying the emission changes and associated air quality impacts during the COVID-19 pandemic on the North China Plain: a response modeling study, Atmos. Chem. Phys., 20, 14347–14359, https://doi.org/10.5194/acp-20-14347-2020, 2020.

Yang, Q., Bitz, C. M., and Doherty, S. J.: Offsetting effects of aerosols on Arctic and global climate in the late 20th century, Atmos. Chem. Phys., 14, 3969-3975, https://doi.org/10.5194/acp-14-3969-2014, 2014.

Zhang, L., Grell, G. A., McKeen, S. A., Ahmadov, R., Froyd, K. D., and Murphy, D.: Inline coupling of simple and complex chemistry modules within the global weather forecast model FIM (FIM-Chem v1), Geosci. Model Dev., 15, 467–491, https://doi.org/10.5194/gmd-15-467-2022, 2022.

Zhang, Q., He, K., and Huo, H.: Cleaning China's air, Nature, 484, 161–162, https://doi.org/10.1038/484161a, 2012.

Zhang, X., Kondragunta, S., da Silva, A., Lu, S., Ding, H., Li, F., and Zhu, Y.: The blended global biomass burning emissions product from MODIS and geostationary satellites (GBBEPx), http://www.ospo.noaa.gov/Products/land/gbbepx/docs/GBBEPx_ATBD.pdf (last access: 1 June 2018), 2014.

Zhang, X., Kondragunta, S., Ram, J., Schmidt, C., and Huang, H.-C.: Near-real-time global biomass burning emissions product from geostationary satellite constellation, J. Geophys. Res., 117, D14201, https://doi.org/10.1029/2012JD017459, 2012.

Zhao, C., Liu, X., Leung, L. R., Johnson, B., McFarlane, S. A., Gustafson Jr., W. I., Fast, J. D., and Easter, R.: The spatial distribution of mineral dust and its shortwave radiative forcing over North Africa: modeling sensitivities to dust emissions and aerosol size treatments, Atmos. Chem. Phys., 10, 8821-8838, https://doi.org/10.5194/acp-10-8821-2010, 2010.

Zhao, T. X., Stowe, L. L., Smirnov, A., Crosby, D., Sapper, J., and McClain, C. R.: Development of a global validation package for satellite oceanic aerosol optical thickness retrieval based on AERONET observations and its application to NOAA/NESDIS operational aerosol retrievals, J. Atmos. Sci., 59, 294–312, 2002.

Table.

Table 1. AERONET site information, the correlation coefficients and root mean square error (RMSE) of GEFS-Aerosols, ICAP and NGACv2 AOD with respect to that of AERONET observation for the period 7/5/2019-11/30/2019. Correlation coefficients are at the 95% confidence interval.

Stations	Station Names	(Latitude, Longitude)	Corr. with GEFS-Aerosols	Corr. with NGACv2	Corr. with ICAP	RMSE with GEFS-Aerosols	RMSE with NGACv2	RMSE with ICAP
1	Dakar	(14.39N, 16.95W)	0.60	0.21	0.78	0.19	0.24	0.10
2	Cape Verde	(16.73N, 22.93W)	0.54	0.39	0.86	0.25	0.27	0.11
3	Banizoumbu	(13.54N, 2.66E)	0.46	0.23	0.81	0.19	0.25	0.14
4	Tamanrassett	(22.79N, 5.53E)	0.40	0.29	0.78	0.26	0.34	0.17
5	Tenerife	(28.47N, 16.24W)	0.55	0.32	0.88	0.17	0.19	0.06
6	Saada	(31.62N, 8.15W)	0.72	0.17	0.83	0.19	0.30	0.10
7	Ben Salem	(35.55N, 9.91E)	0.74	0.15	0.86	0.08	0.29	0.07
8	Sede Boker	(30.85N, 34.78E)	0.72	0.16	0.83	0.10	0.20	0.07
9	Dewa	(24.76N, 55.36E)	0.47	0.41	0.85	0.29	0.30	0.13
10	Granada	(37.16N, 3.60W)	0.82	0.32	0.77	0.08	0.13	0.08
11	Cape San Juan	(18.38N, 65.62W)	0.43	0.28	0.64	0.14	0.21	0.04
12	Dushanbe	(38.55N, 68.85E)	0.29	0.14	0.60	0.32	0.33	0.25
13	Dalanzadgaad	(43.57N,104.41E)	0.71	0.46	0.81	0.13	0.16	0.10
14	Bejing	(39.97N,116.38E)	0.67	0.47	0.80	0.43	0.68	0.33
15	Kanpur	(26.51N, 80.23E)	0.76	0.15	0.87	0.36	0.51	0.32
16	Kyiv	(50.36N, 30.49E)	0.45	0.18	0.62	0.14	0.20	0.06
17	Barcelona	(41.38N, 2.11E)	0.62	0.39	0.76	0.12	0.16	0.08
18	Leipzig	(51.35N, 12.43E)	0.77	0.20	0.80	0.11	0.13	0.05
19	Sochengcho	(37.42N,124.73E)	0.63	0.63	0.74	0.31	0.47	0.24
20	Singapore	(1.29N,103.78E)	0.40	0.19	0.62	0.66	0.89	0.36
21	Reunion St Denis	(20.90S, 55.48E)	0.42	0.46	0.74	0.05	0.08	0.05
22	Lumbini	(27.50N, 83.28E)	0.44	0.32	0.58	0.28	0.29	0.29
23	Cape Fuguei	(25.29N,121.53E)	0.66	0.33	0.63	0.37	0.66	0.34
24	Lake Argyle	(16.10S,128.74E)	0.60	0.37	0.78	0.06	0.06	0.05
25	Chilbolton	(51.14N, 1.43W)	0.66	0.20	0.79	0.09	0.12	0.05
26	Opal	(79.99N, 85.93W)	0.19	0.13	0.61	0.12	0.16	0.08
27	Resolute Bay	(74.70N, 94.96W)	0.28	0.21	0.62	0.11	0.11	0.06
28	Thule	(76.51N, 68.76W)	0.32	0.13	0.57	0.12	0.13	0.07
29	Kangerlussuaq	(66.99N, 50.62W)	0.83	0.35	0.97	0.09	0.10	0.05
30	Tomsk	(56.45N, 85.04E)	0.72	0.18	0.83	0.55	0.79	0.27
31	Hornsund	(77.0N, 15.54E)	0.66	0.68	0.90	0.13	0.16	0.07
32	Alta Floresta	(9.87S, 56.10W)	0.81	0.30	0.88	0.24	0.34	0.12
33	Santa Cruz Utepsa	(17.76S, 63.20W)	0.86	0.45	0.94	0.21	0.42	0.13
34	Itajuba	(22.41S, 45.45W)	0.43	0.25	0.57	0.17	0.24	0.09
35	La Paz	(16.53S, 68.06W)	0.48	0.19	0.79	0.07	0.12	0.08
36	SEGS Lope Gabon	(0.202S, 11.60E)	0.71	0.43	0.94	0.29	0.69	0.39
37	Ascension Island	(7.97S, 14.41W)	0.54	0.45	0.33	0.13	0.25	0.08
38	Bamenda	(5.94N, 10.15E)	0.67	0.59	0.94	0.17	0.17	0.47
39	Mongu Inn	(15.26S, 23.13E)	0.72	0.15	0.86	0.17	0.32	0.17
40	Misamfu	(10.17S, 31.22E)	0.80	0.38	0.83	0.17	0.35	0.15
41	Maun Tower	(19.9S, 23.55E)	0.66	0.26	0.85	0.10	0.22	0.11
42	Windpoort	(19.36S, 15.48E)	0.64	0.33	0.69	0.18	0.29	0.09
43	Lubango	(14.95S, 13.44E)	0.81	0.72	0.54	0.16	0.32	0.14
44	Bonanza Creek	(64.74N,148.31W)	0.77	0.21	0.70	0.32	0.60	0.23
45	Fort McMurray	(56.75N,111.47W)	0.72	0.14	0.71	0.16	0.29	0.12
46	Chapais	(49.82N, 74.97W)	0.32	0.11	0.55	0.11	0.14	0.07
47	Saturn Island	(48.77N,123.12W)	0.63	0.28	0.76	0.09	0.09	0.05
48	Missoula	(46.91N,114.08W)	0.43	0.14	0.79	0.09	0.11	0.04

49	Camaguey	(21.42N, 77.85W)	0.63	0.16	0.82	0.06	0.12	0.04
50	Neon Wood	(47.12N, 99.24W)	0.58	0.18	0.75	0.10	0.16	0.06
51	GSFC	(38.99N, 76.84W)	0.47	0.15	0.77	0.08	0.16	0.06
52	Monterey	(36.59N,121.85W)	0.39	0.32	0.66	0.04	0.04	0.03
53	Toronto	(43.79N, 79.47W)	0.66	0.17	0.52	0.15	0.19	0.10
54	Red Mountain Pass	(37.90N,107.71W)	0.65	0.15	0.76	0.03	0.04	0.02
55	Tucson	(32.23N,110.95W)	0.62	0.16	0.81	0.05	0.08	0.03
56	Appalachian State	(36.21N, 81.69W)	0.69	0.11	0.75	0.07	0.13	0.05
57	Cartel	(45.38N, 71.93W)	0.08	0.19	0.26	0.09	0.13	0.06
58	Mauna Loa	(19.53N,155.57W)	0.35	0.20	0.79	0.05	0.04	0.04
59	ARM SGP	(36.6N, 97.48W)	0.64	0.26	0.64	0.08	0.14	0.05
60	Univ. of Wisconsin	(43.07N, 89.41W)	0.60	0.21	0.78	0.06	0.08	0.05

Table 2. Comparison of model configurations between GEFS-Aerosols and NGACv2

Mode Configurations	**GEFS-Aerosols**	**NGACv2**
Atmospheric model	FV3	NEMS GSM
Physics package	GFS v15	GFS v2015
Horizontal resolution	~25 km	~100 km
Vertical resolution	64 layers	64 layers
Coupled infrastructure	NUOPC	ESMF
Anthropogenic Emission	CEDS 2014	EDGAR v4.1
Fire Emission	GBBEPx v3	GBBEPx and QFED v2
Aerosol scheme for BC, OC, sulfate and sea salt	GOCART	GOCART
Dust scheme	FENGSHA	GOCART

Table 3. ATom-1 column sum statistics of mean bias and correlation for sulfate, OC, EC and dust.

Species	N	Obs. median (mg/m^2)	FV3-C384 MMO	NGAC-v2 MMO	FV3-C384 r-coeff.	NGAC-v2 r-coeff.
Sulfate	153	0.58	0.72	-	0.63	-
Organic Carbon	146	0.55	1.03	-	0.80	-
Elemental Carbon	152	0.011	3.35	-	0.78	-
Dust (< 3. μm diam)	130	0.038	0.54	46.37	0.39	0.39

N is the sample number, MMO stands for Median Model to Observed Ratio, and r-coeff. is the Pearson correlation r-coefficient.

Figure Captions.

Figure 1. Diagram showing the GSDCHEM component within the NEMS infrastructure.

Figure 2. (a) Diagram of GEFS-Aerosols coupled structure; (b) Flowchart of steps/tasks for GEFS-Aerosols in the global workflow forecast system.

Figure 3. Anthropogenic emissions of CEDS (2014) and HTAP (2010) for SO_2 (mole/km^2/hr), BC and OC (ng/m^2/s) on summer of July.

Figure 4. Total AOD forecast on 25th August compared with the NGAC model, MERRA2 reanalysis data and satellite observations of VIIRS and MODIS. The 18z forecasts from both models for that day and daily satellite data are used in the figure. Satellite data gaps are in white.

Figure 5. Correlation coefficients and RMSE between AERONET daily total AOD observations and GEFS-Aerosols, ICAP and NGAC for the period 7/5/19-11/30/19. Correlation coefficients are at the 95% confidence interval.

Figure 6. Day 1 AOD prediction averaged during 7/5/19-11/30/19 of GEFS-Aerosols and NGAC compared with MERRA-2 reanalysis and MODIS.

Figure 7. Day 1 AOD forecast biases of GEFS-Aerosols and NGAC compared with MERRA-2 averaged during 7/5/19-11/30/19 for dust, OC and sulfate.

Figure 8. Differences of GEFS-Aerosols and NGAC Day 1 predictions of total AOD compared with MERRA-2 reanalysis averaged during 7/5/19-11/30/19.

Figure 9. Day 1 AOD forecasts of GEFS-Aerosols, ICAP, and NGAC verified against AERONET sites in South America during 7/5/19-11/30/19.

Figure 10. Day 1 AOD forecasts of GEFS-Aerosols, ICAP, and NGAC verified against AERONET sites in Africa during 7/5/19-11/30/19.

Figure 11. Day 1 AOD forecasts of GEFS-Aerosols, ICAP, and NGAC verified against AERONET sites in dust source regions and surrounding downwind areas during 7/5/19-11/30/19.

Figure 12. Daily AERONET total AOD versus modeled total AOD from GEFS-Aerosols (blue) and NGAC (orange) at the AERONET sites of (a) Tamanrassett, (b) Cape Verde, and (c) Tenerife with linear regression fits.

Figure 13. GEFS-Aerosols and NGAC day 1 total AOD forecast time series against MERRA-2 reanalysis data averaged over major global regions of North Africa (0°-35°N, 18°W-30°E), North Atlantic Ocean, (0°-40°N, 10°-80°W), Southern Africa (0°-35°S, 8°-35°E), South Atlantic (0°-35°S, 40°W-20°E), South America (0°-35°S, 35°W-80°W), Europe (35°-65°N, 10°W-50°E), East Asia (20°-48°N, 100°-140°E), Eastern USA (25°-48°N, 68°-95°W), and Western USA (25°- 48°N, 95°-125°W).

Figure 14. Tropospheric column sums of OC for (a) NASA DC-8 observations; and (b) GEFS-Aerosols.

Figure 15. Tropospheric column sums of dust for (a) the NASA DC-8 observations; (b) GEFS-Aerosols; and (c) NGAC.

Figure 16. Vertically resolved statistical comparisons of OC, BC and sulfate for the DC-8 flight tracks over the Pacific (July 29-August 8) and Atlantic (August 15-23). Red line is with GEFS-Aerosols.

Figure 17. Vertically resolved statistical comparisons of dust and sea salt for the DC-8 flight tracks over the Pacific (July 29-August 8) and Atlantic (August 15-23). Red line is GEFS-Aerosols, green line is NGAC.

Figure 18. Height-latitude profiles of OC, EC and sulfate over Atlantic on August 15 and 17th, 2016 for (a) the ATom-1 DC-8 observations; (b) GEFS-Aerosols.

Figure 19. Height-latitude profiles of dust and sea salt over Atlantic on August 15 and 17th, 2016 for (a) the ATom-1 DC-8 observations; (b) GEFS-Aerosols and (c) NGAC.

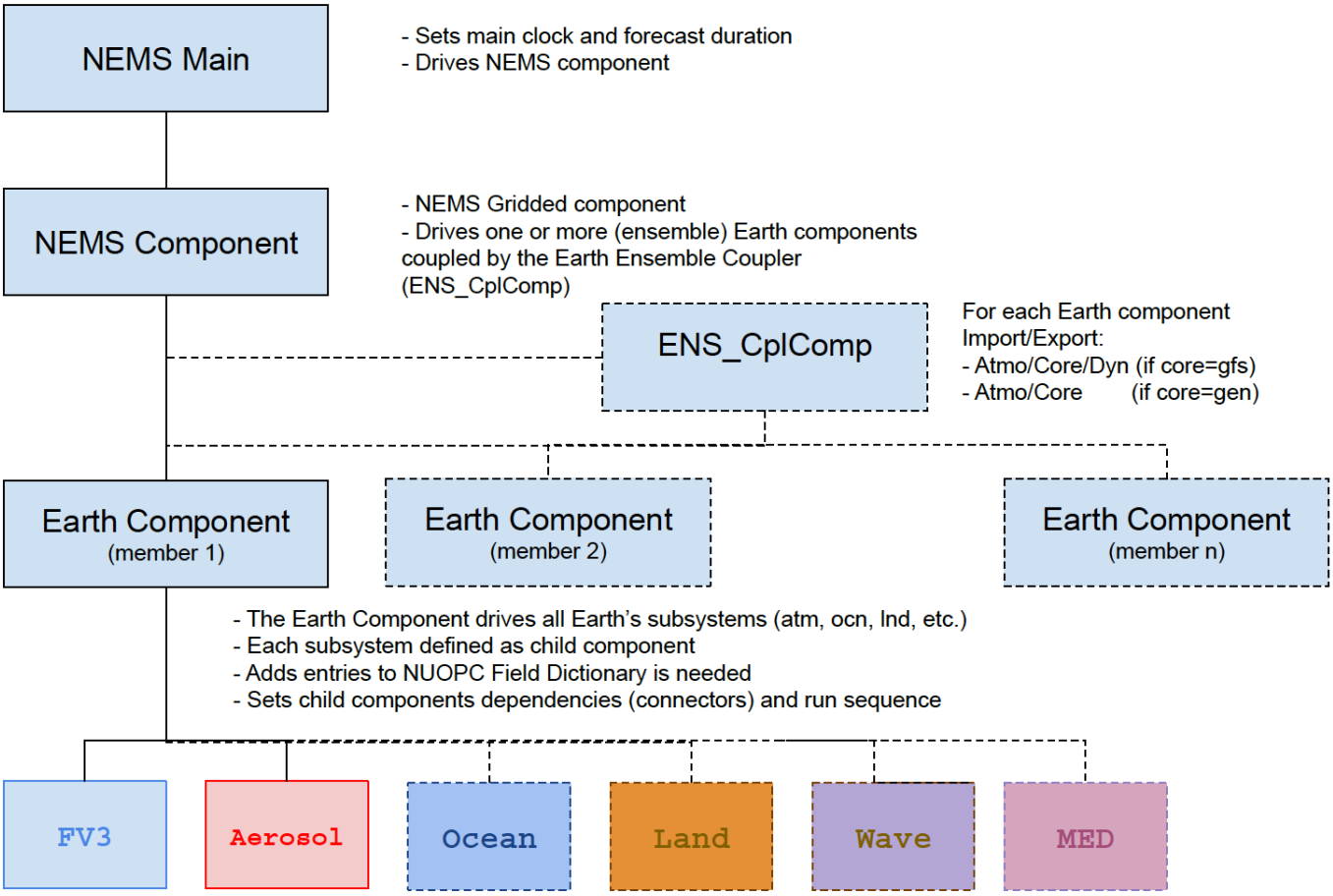

Figure 1. Diagram showing the GSDCHEM component within the NEMS infrastructure.

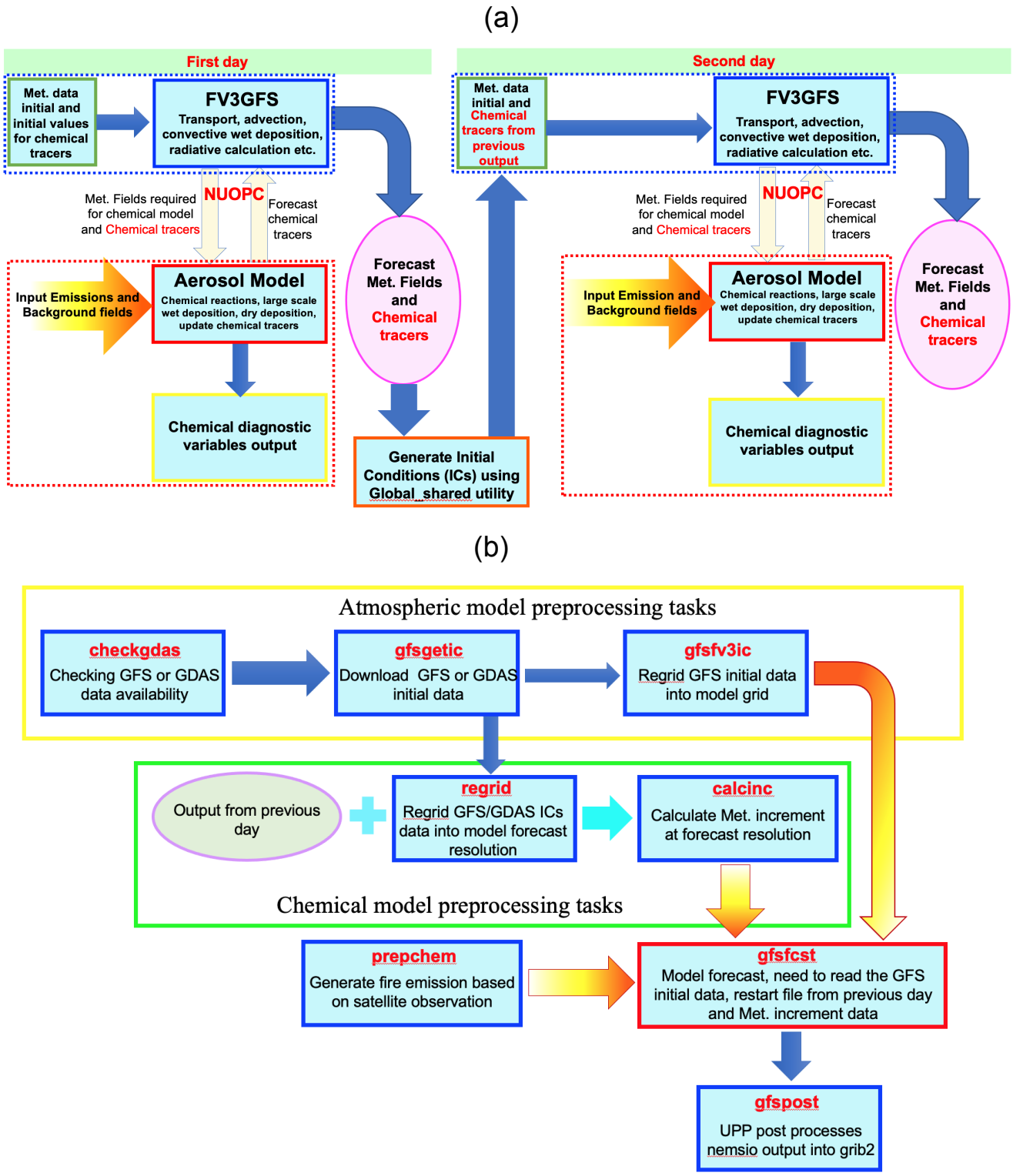

Figure 2. (a) Diagram of GEFS-Aerosols coupled structure; (b) Flowchart of steps/tasks for GEFS-Aerosols in the global workflow forecast system.

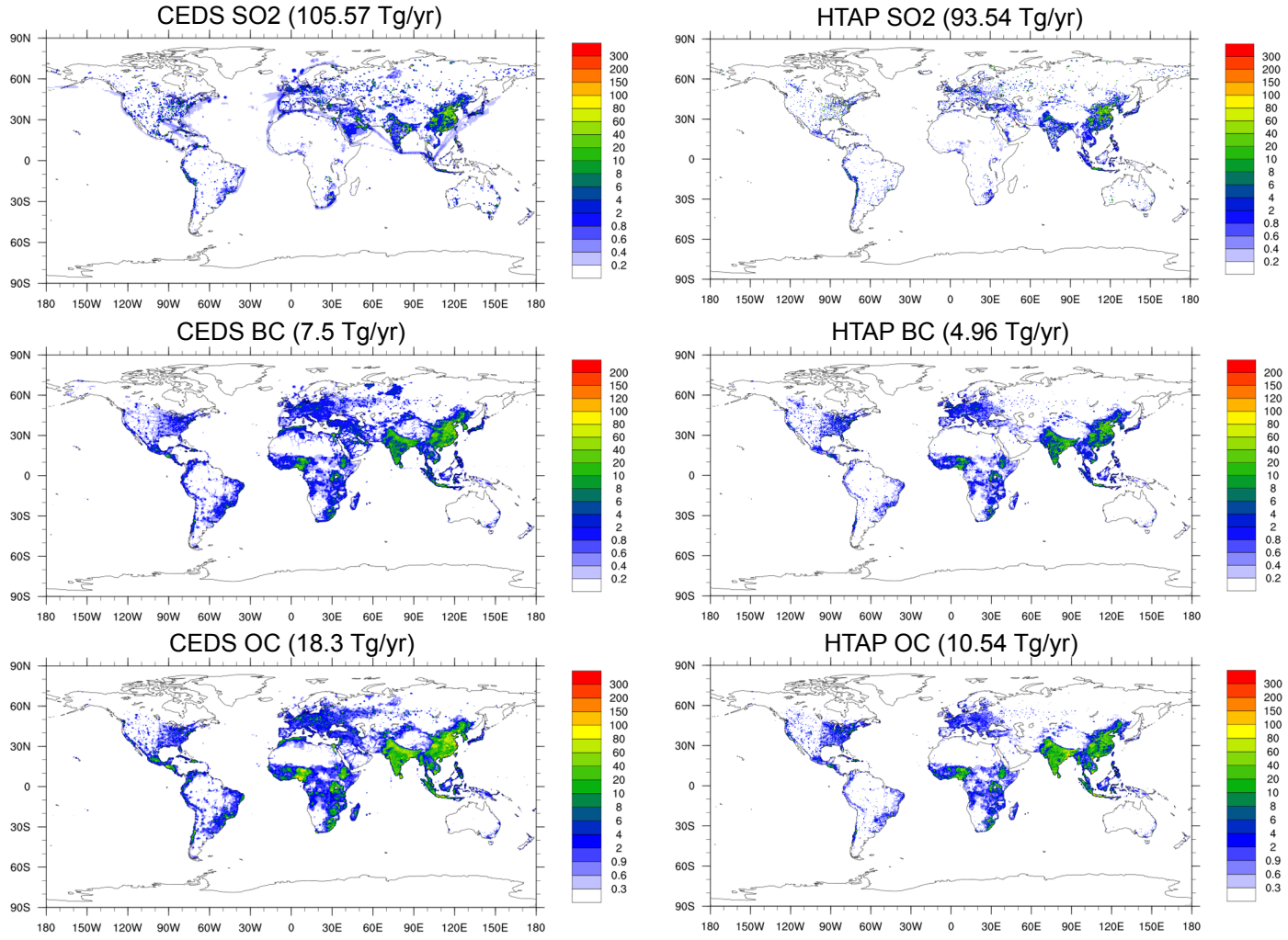

Figure 3. Anthropogenic emissions of CEDS (2014) and HTAP (2010) for SO2 (mole/km2/hr), BC and OC (ng/m2/s) on summer of July.

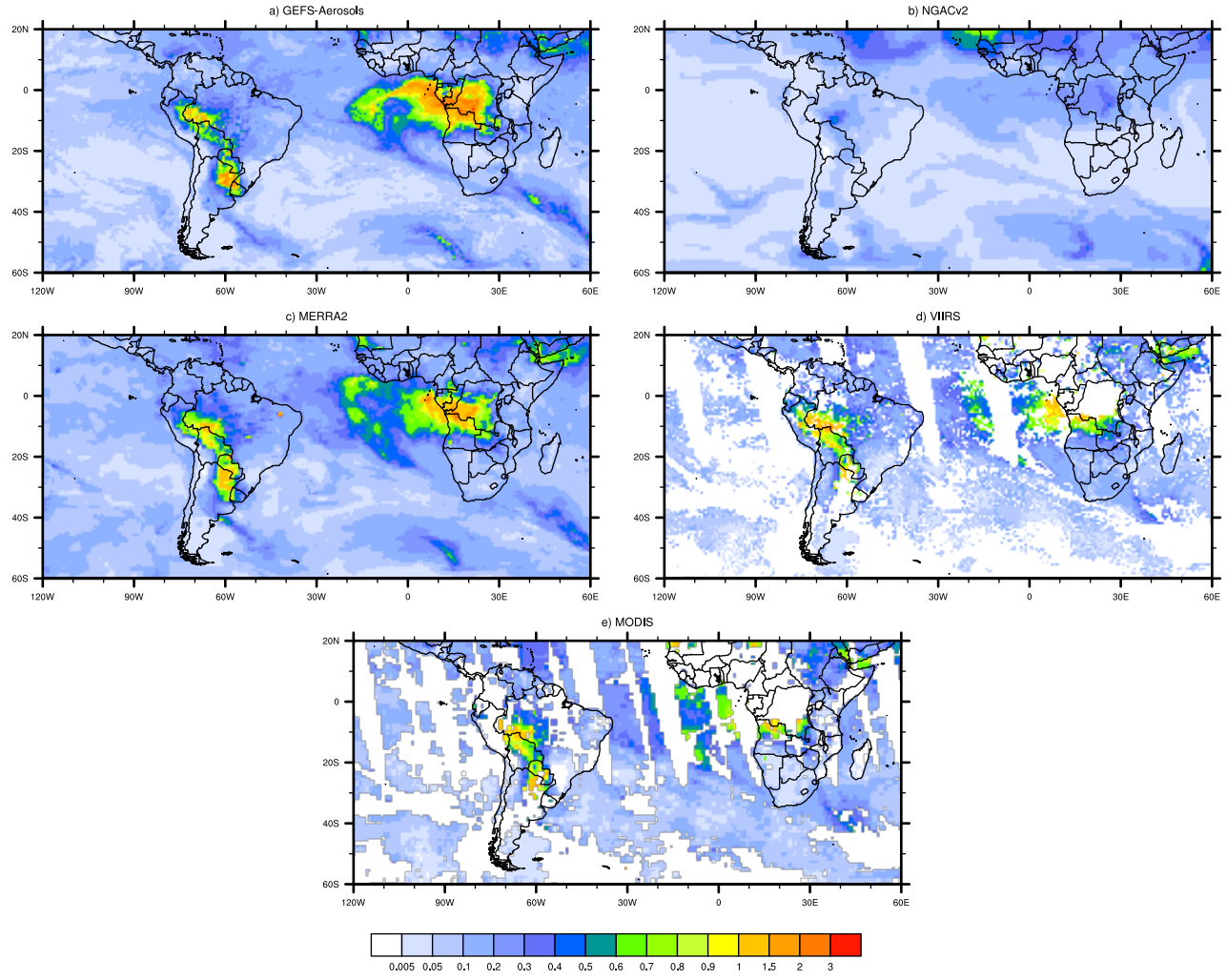

Figure 4. Total AOD forecast on 25th August verified against the NGAC model, MERRA2 reanalysis data and satellite observations of VIIRS and MODIS. The 18z forecasts from both models for that day and daily satellite data are used in the figure. Satellite data gaps are in white.

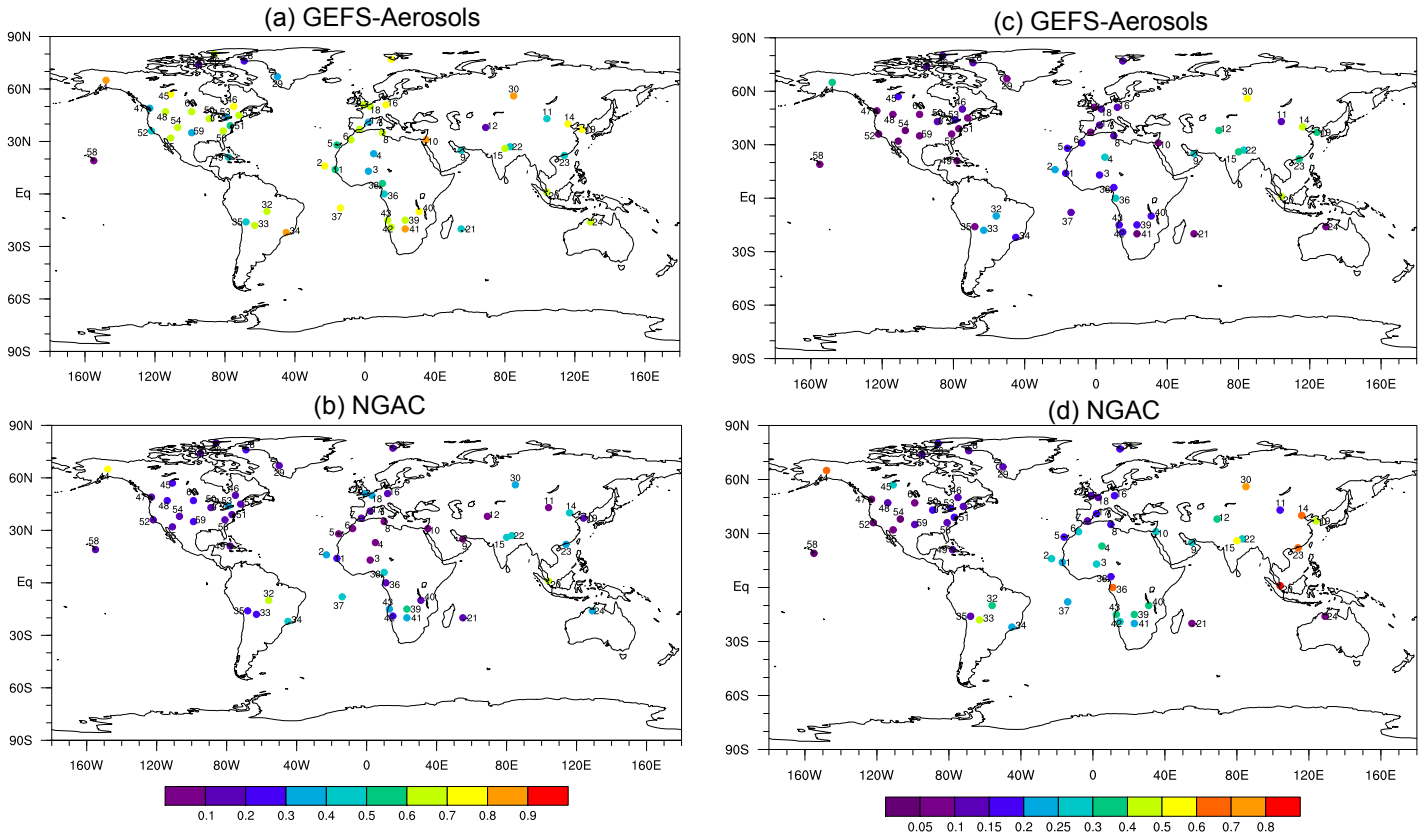

Figure 5. Correlation coefficients and RMSE between AERONET daily total AOD observations and model predictions by GEFS-Aerosols and NGAC for the period 7/5/19-11/30/19. Correlation coefficients are at the 95% confidence interval.

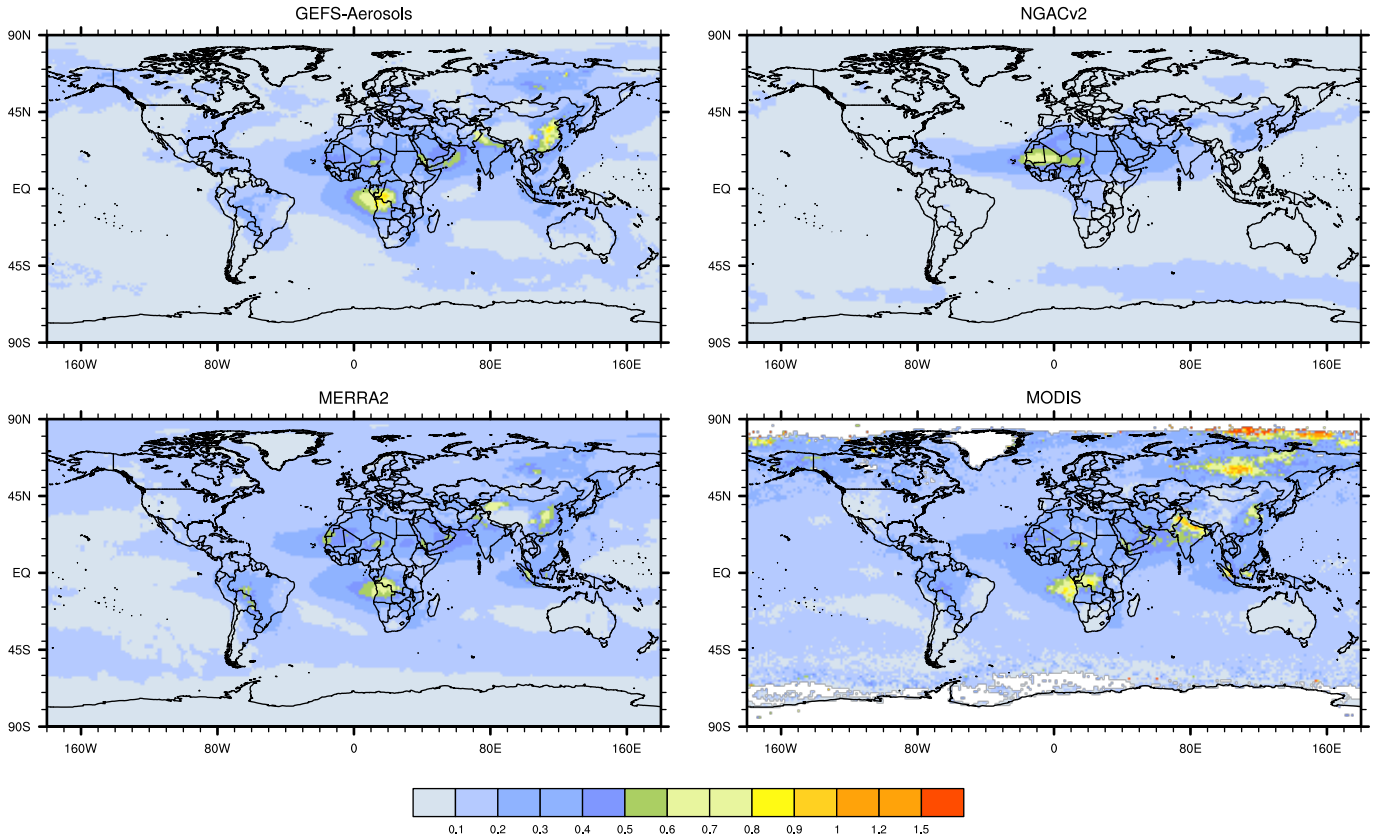

Figure 6. Day 1 AOD prediction of GEFS-Aerosols and NGAC compared with MERRA-2 reanalysis and MODIS averaged during 7/5/19-11/30/19.

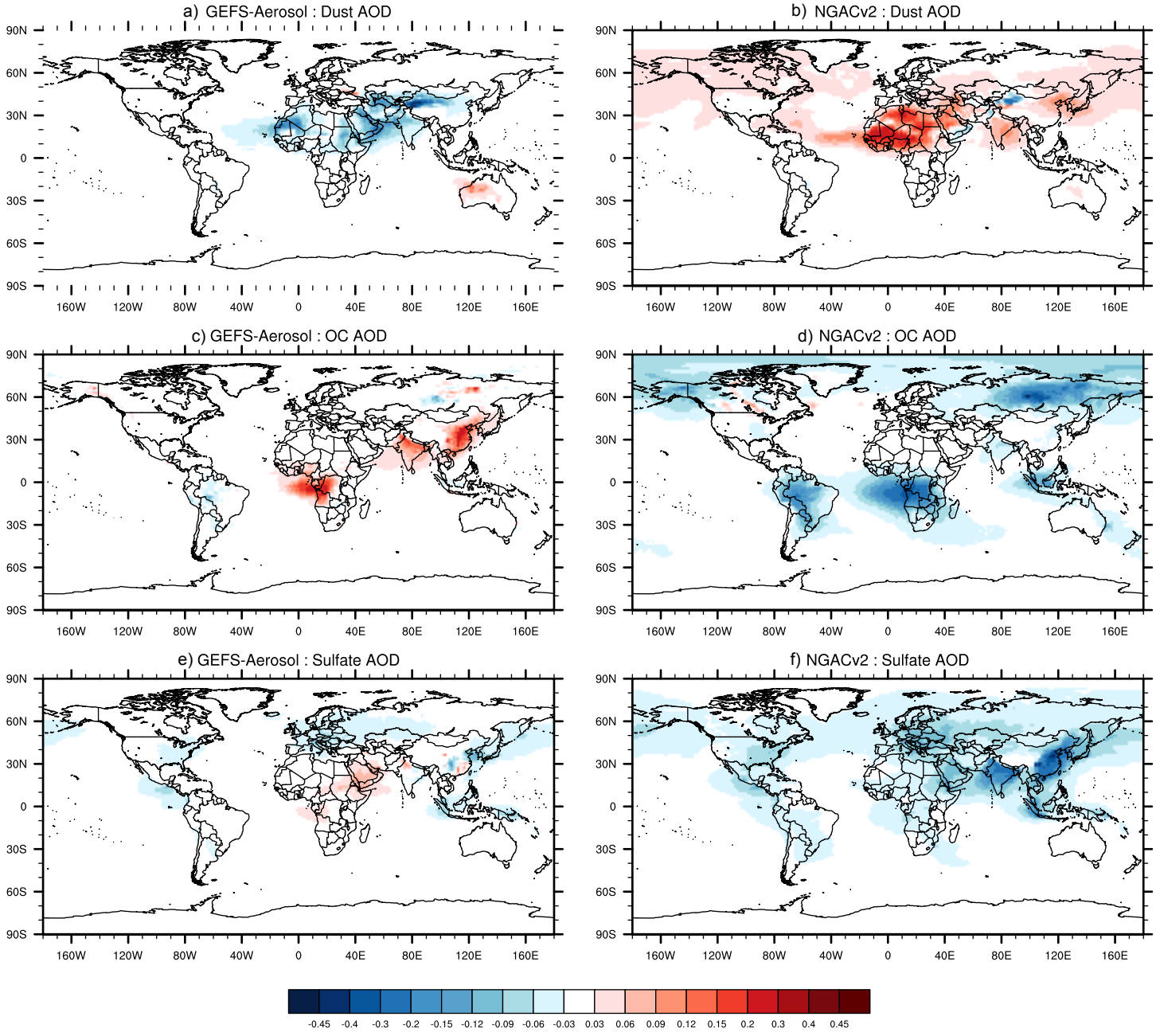

Figure 7. Day 1 AOD forecast biases of GEFS-Aerosols and NGAC compared with MERRA-2 averaged during 7/5/19-11/30/19 for dust, OC and sulfate.

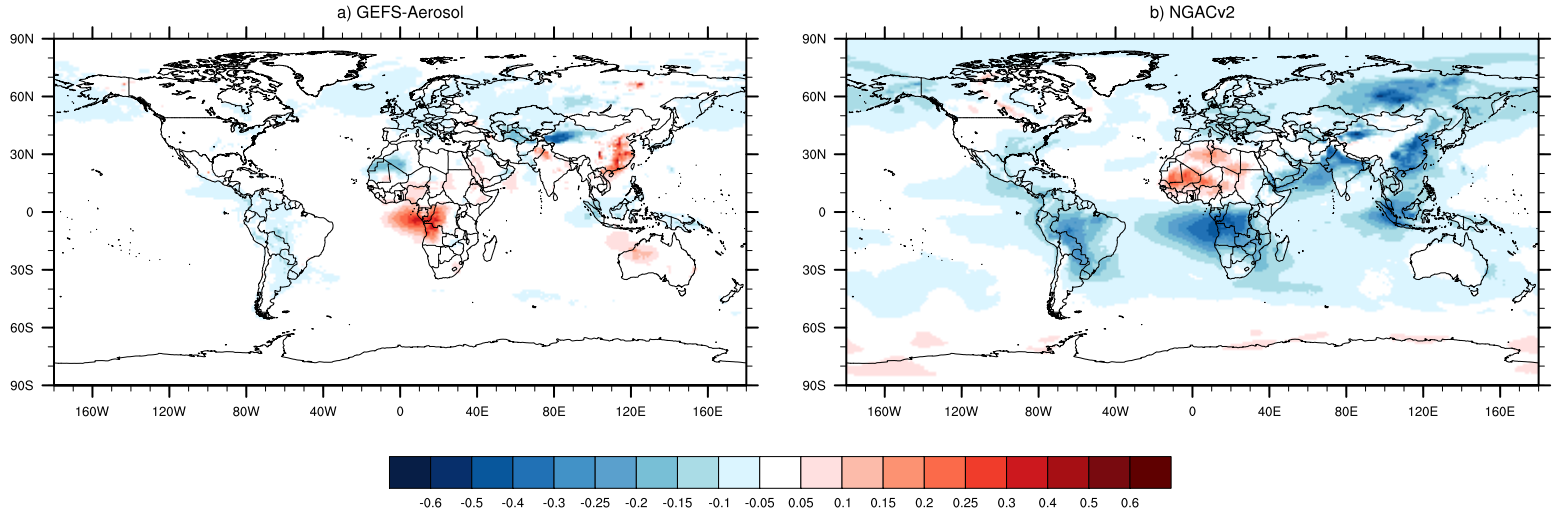

Figure 8. Differences of GEFS-Aerosols and NGAC Day 1 predictions of total AOD compared with MERRA-2 reanalysis averaged during 7/5/19-11/30/19.

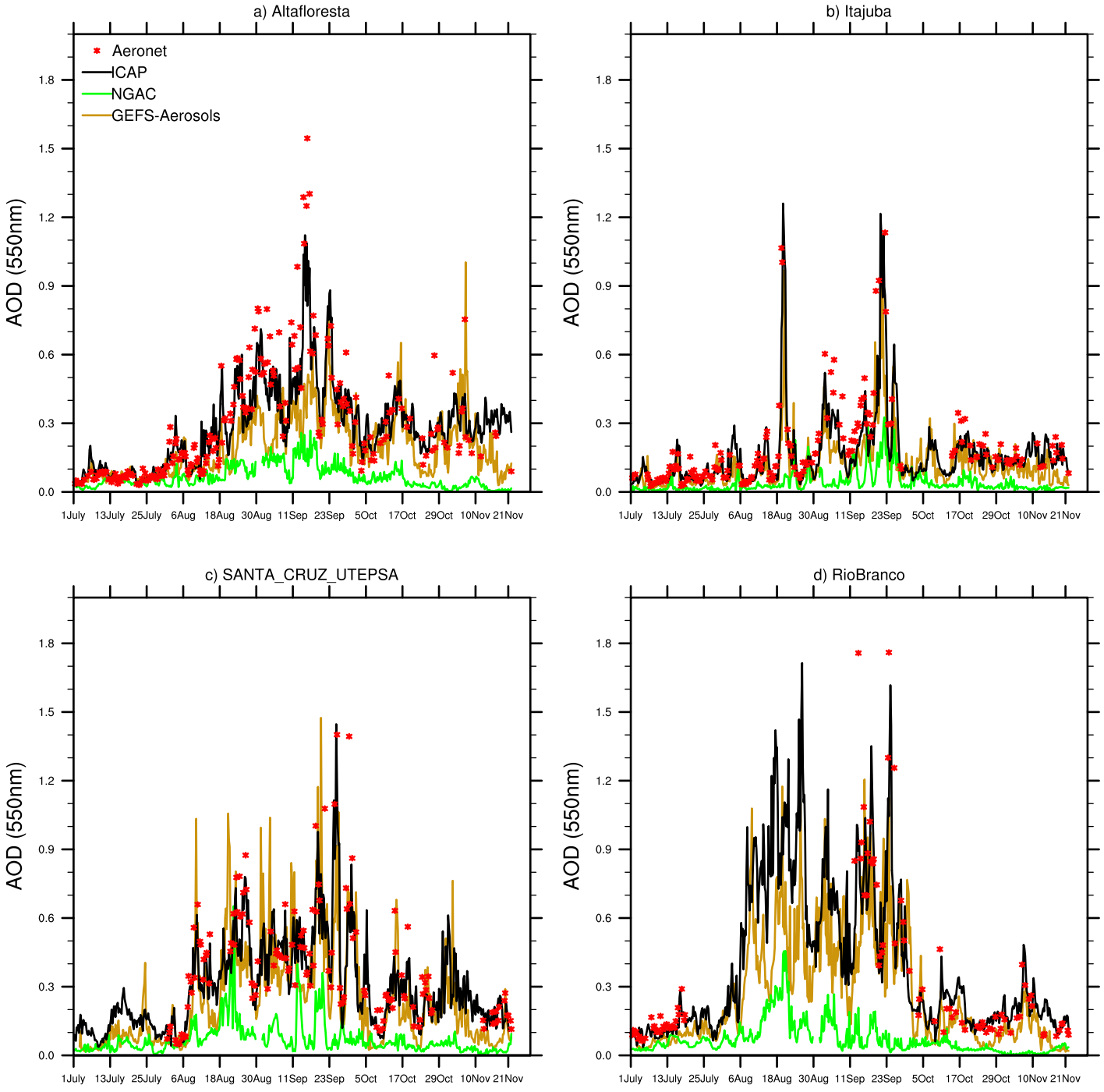

Figure 9. Day 1 AOD forecasts of GEFS-Aerosols, ICAP, and NGAC verified against AERONET sites in South America during 7/5/19-11/30/19.

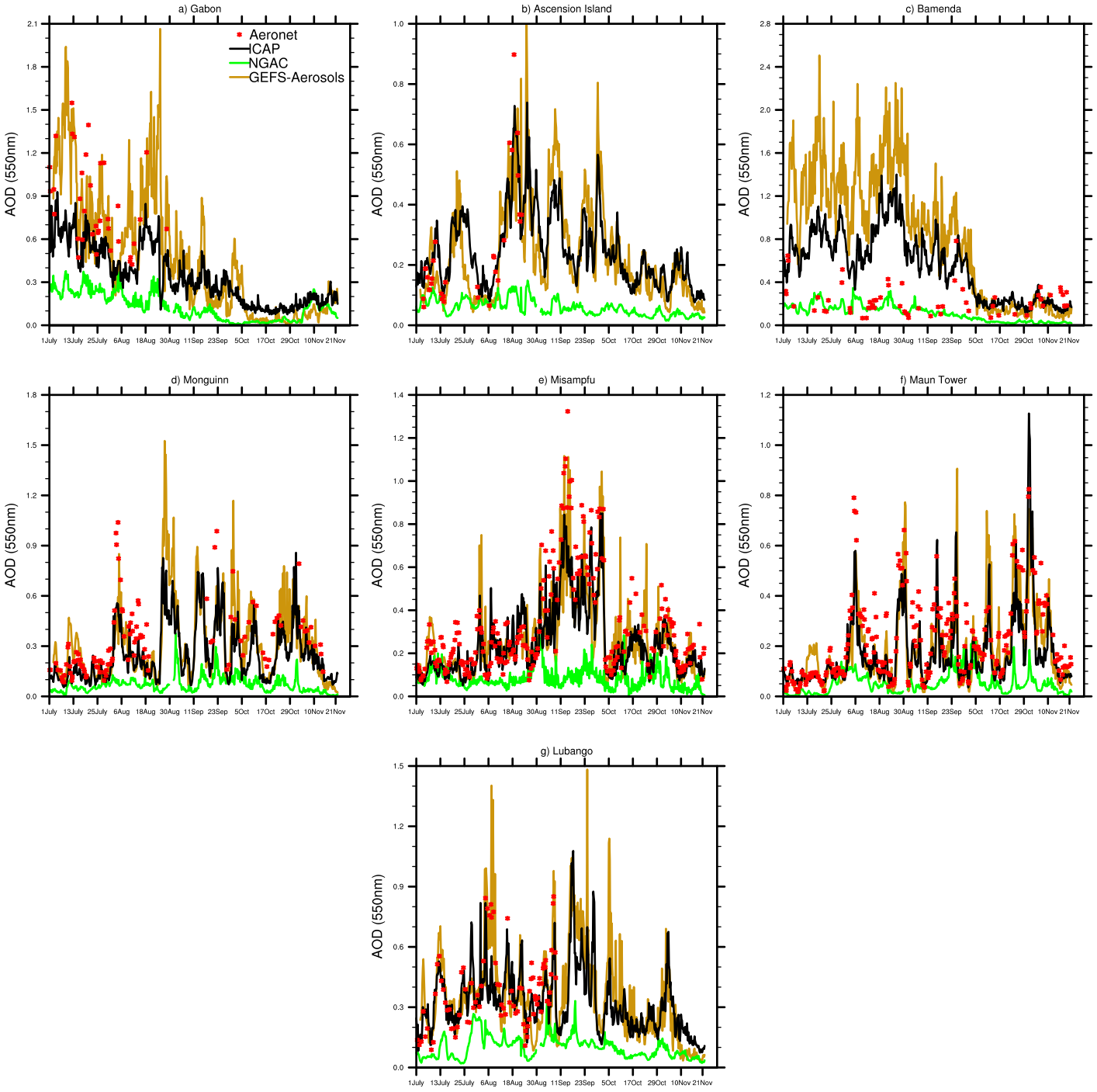

Figure 10. Day 1 AOD forecasts of GEFS-Aerosols, ICAP, and NGAC verified against AERONET sites in Africa during 7/5/19-11/30/19.

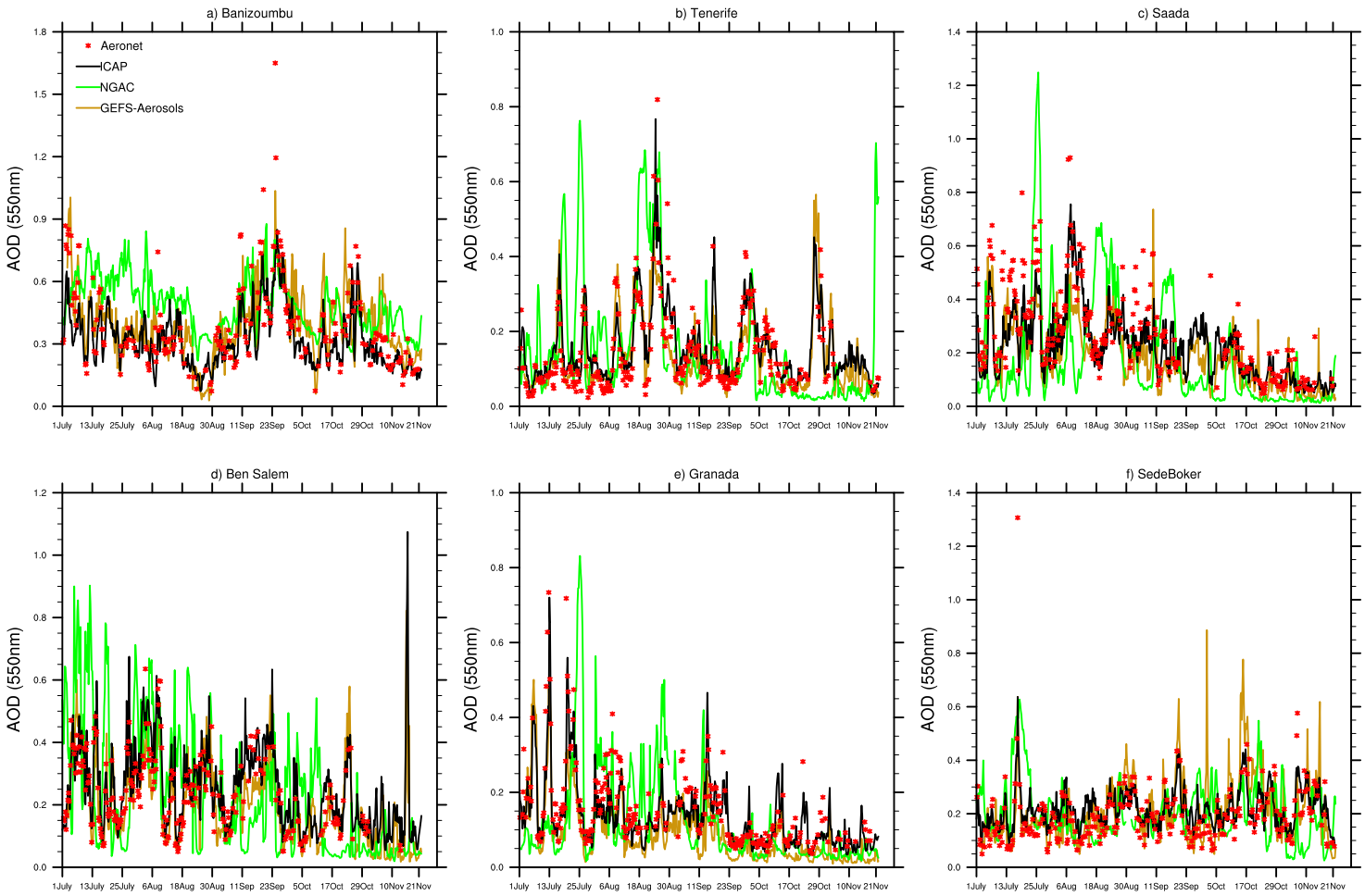

Figure 11. Day 1 AOD forecasts of GEFS-Aerosols, ICAP, and NGAC verified against AERONET sites in dust source regions and surrounding downwind areas during 7/5/19-11/30/19.

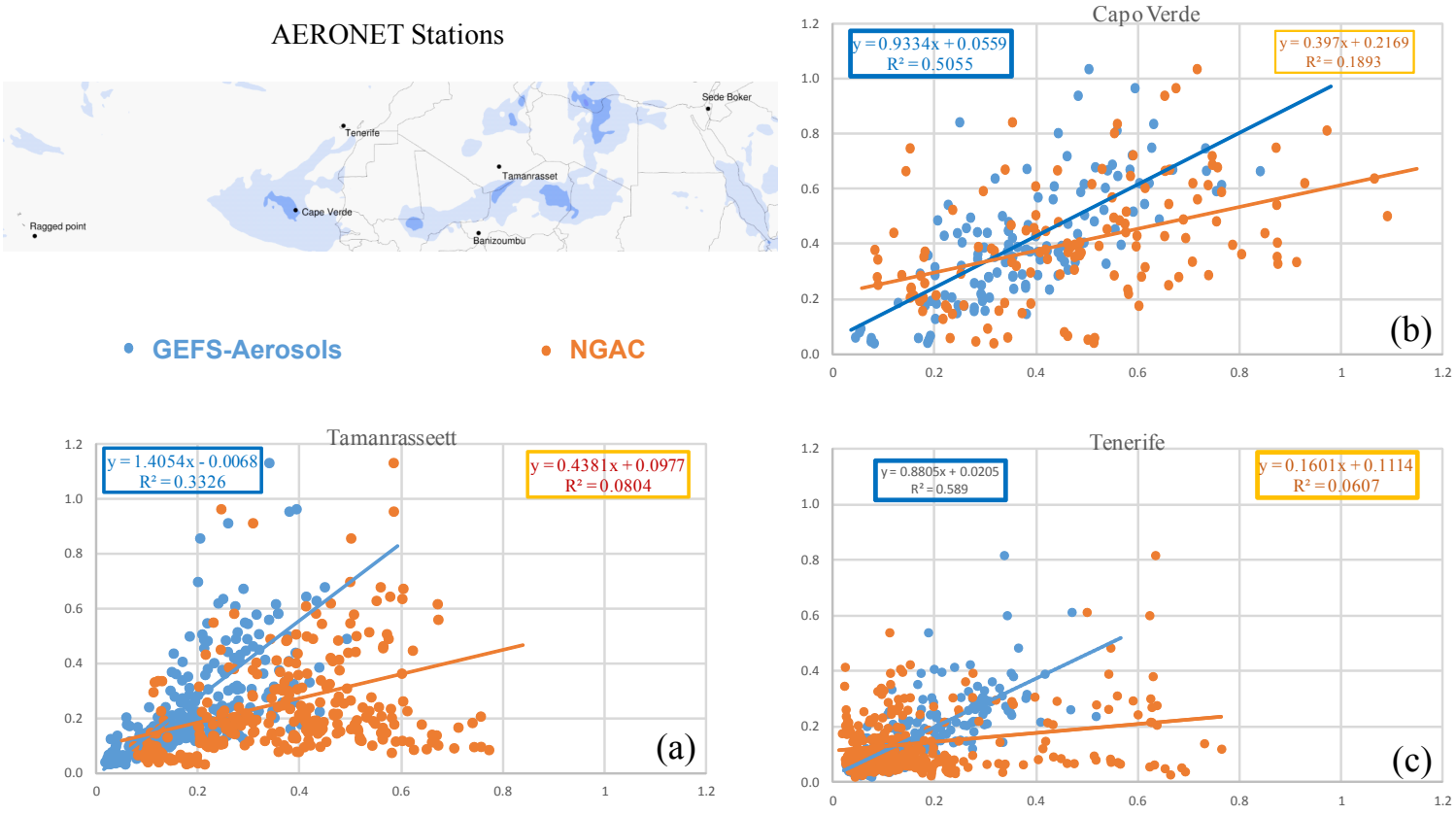

Figure 12. Daily AERONET total AOD versus modeled total AOD from GEFS-Aerosols (blue) and NGACv2 (orange) at the AERONET sites of (a) Tamanrassett, (b) Cape Verde, and (c) Tenerife with linear regression fits.

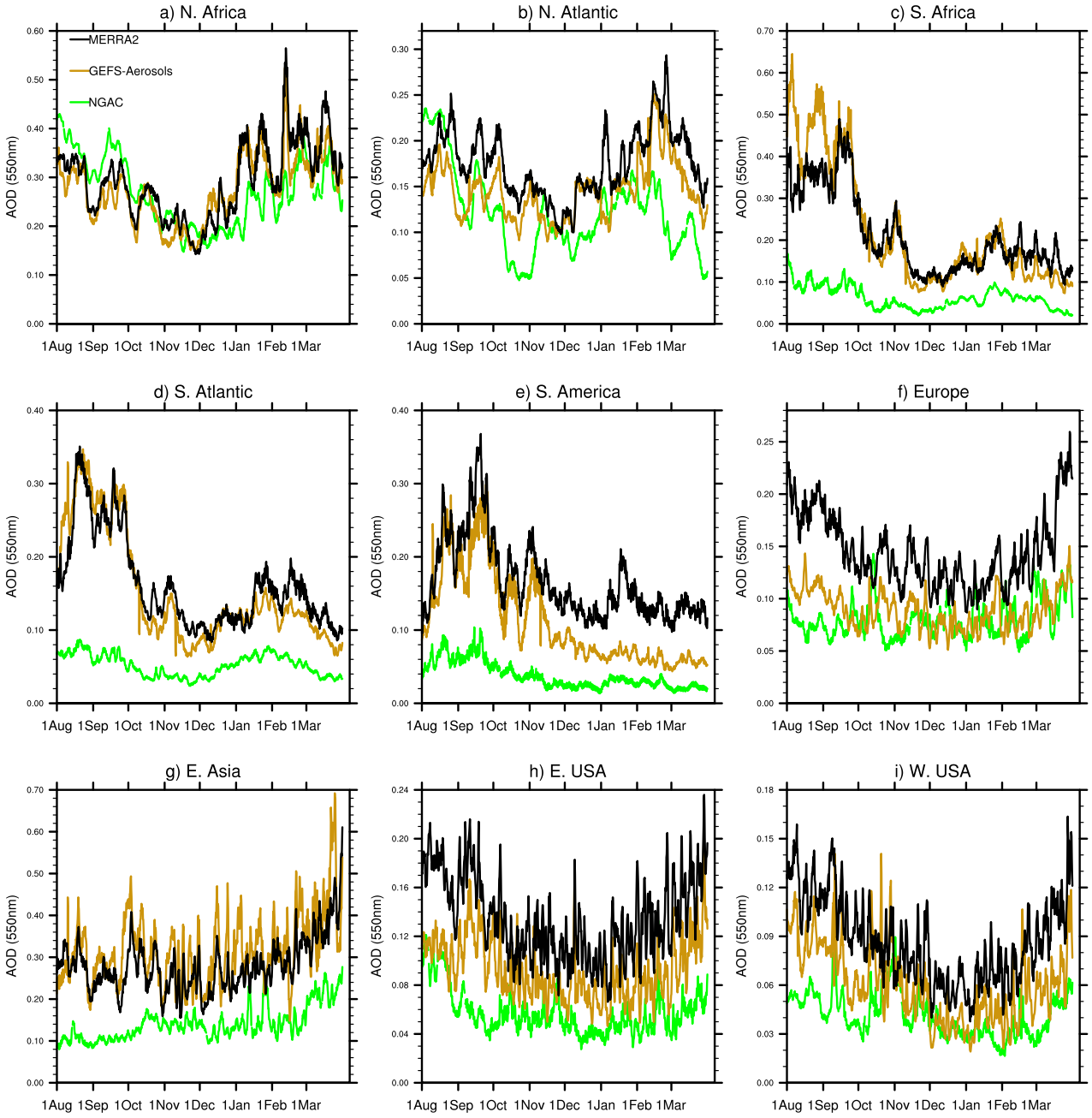

Figure 13. GEFS-Aerosols and NGACv2 day 1 total AOD forecast time series against MERRA-2 reanalysis data averaged over major global regions of North Africa (0°-35°N, 18°W-30°E), North Atlantic Ocean, (0°-40°N, 10°-80°W), Southern Africa (0°-35°S, 8°-35°E), South Atlantic (0°-35°S, 40°W-20°E), South America (0°-35°S, 35°W-80°W), Europe (35°-65°N, 10°W-50°E), East Asia (20°-48°N, 100°-140°E), Eastern USA (25°-48°N, 68°-95°W), and Western USA (25°- 48°N, 95°-125°W).

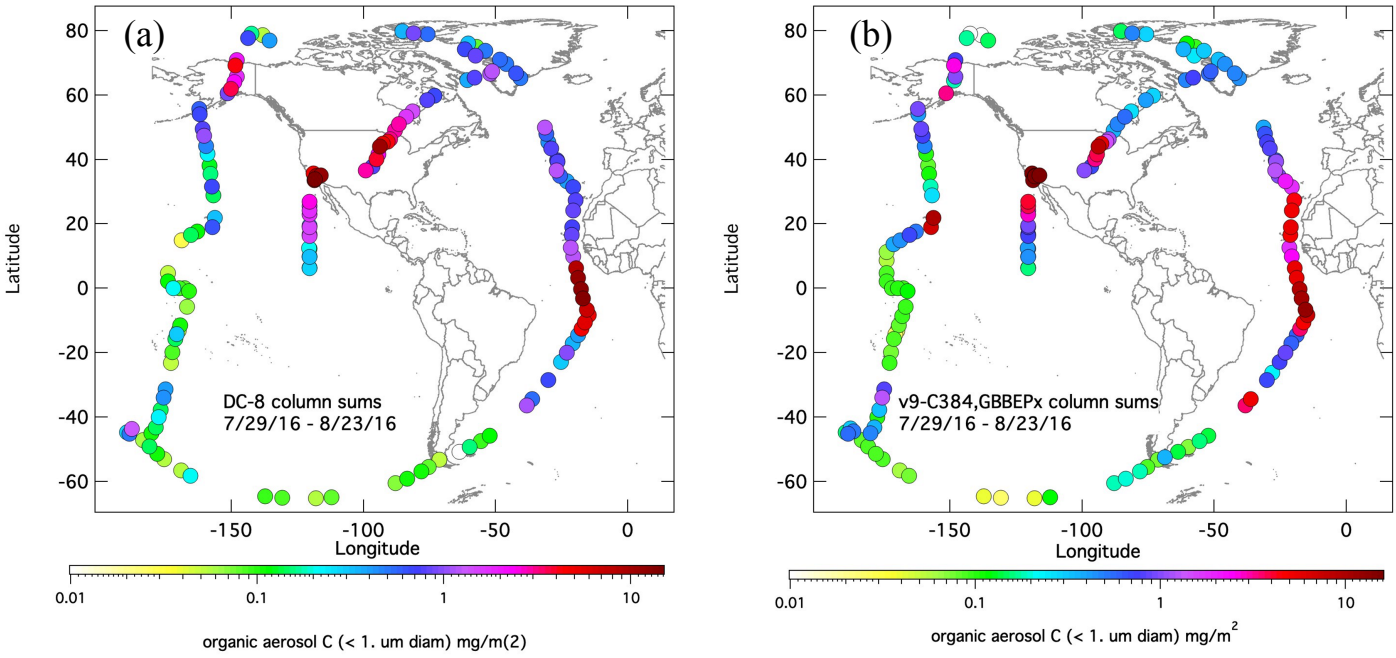

Figure 14. Tropospheric column sums of OC for (a) NASA DC-8 observations; and (b) GEFS-Aerosols.

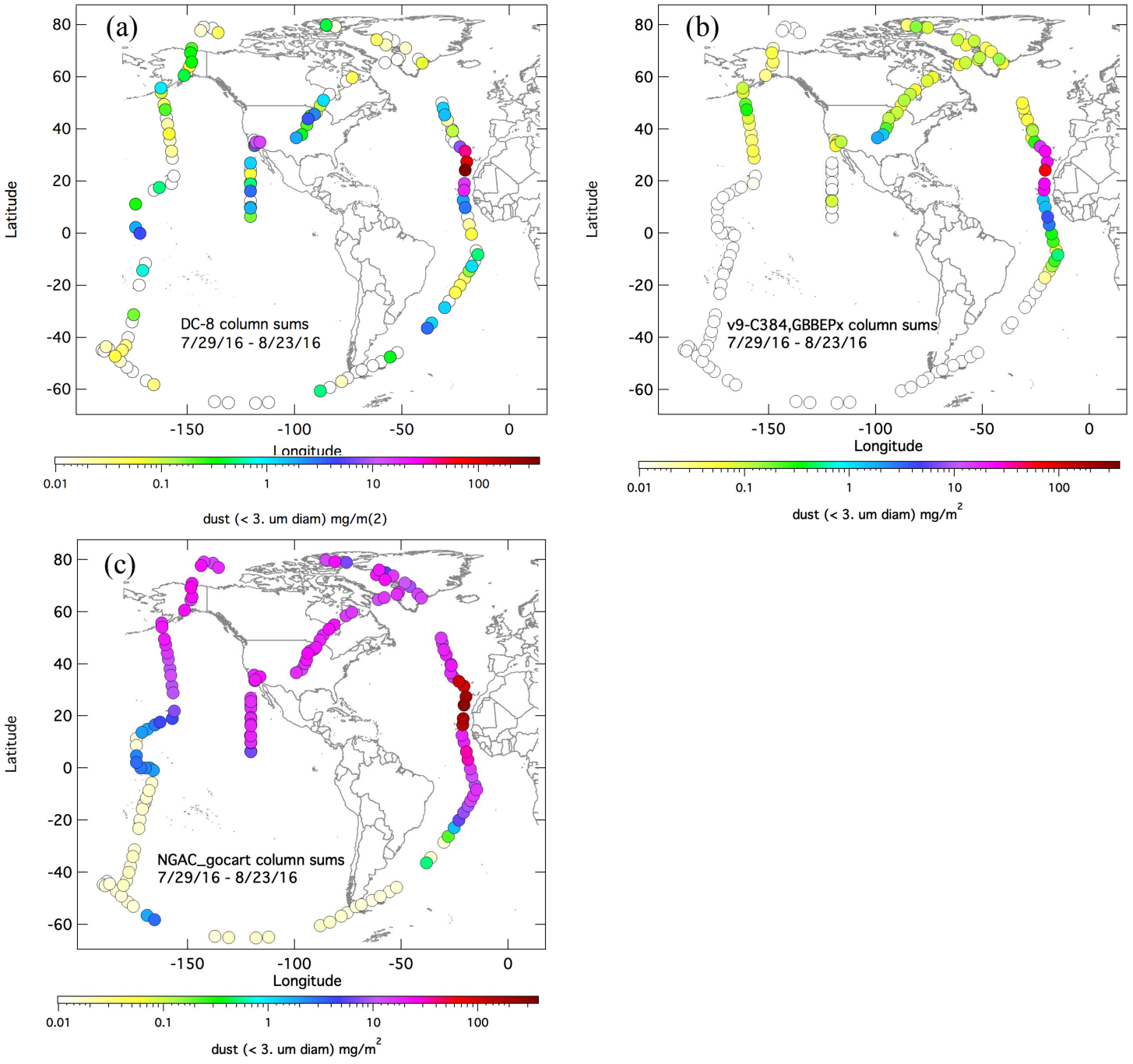

Figure 15. Tropospheric column sums of dust for (a) the NASA DC-8 observations; (b) GEFS-Aerosols; and (c) NGAC.

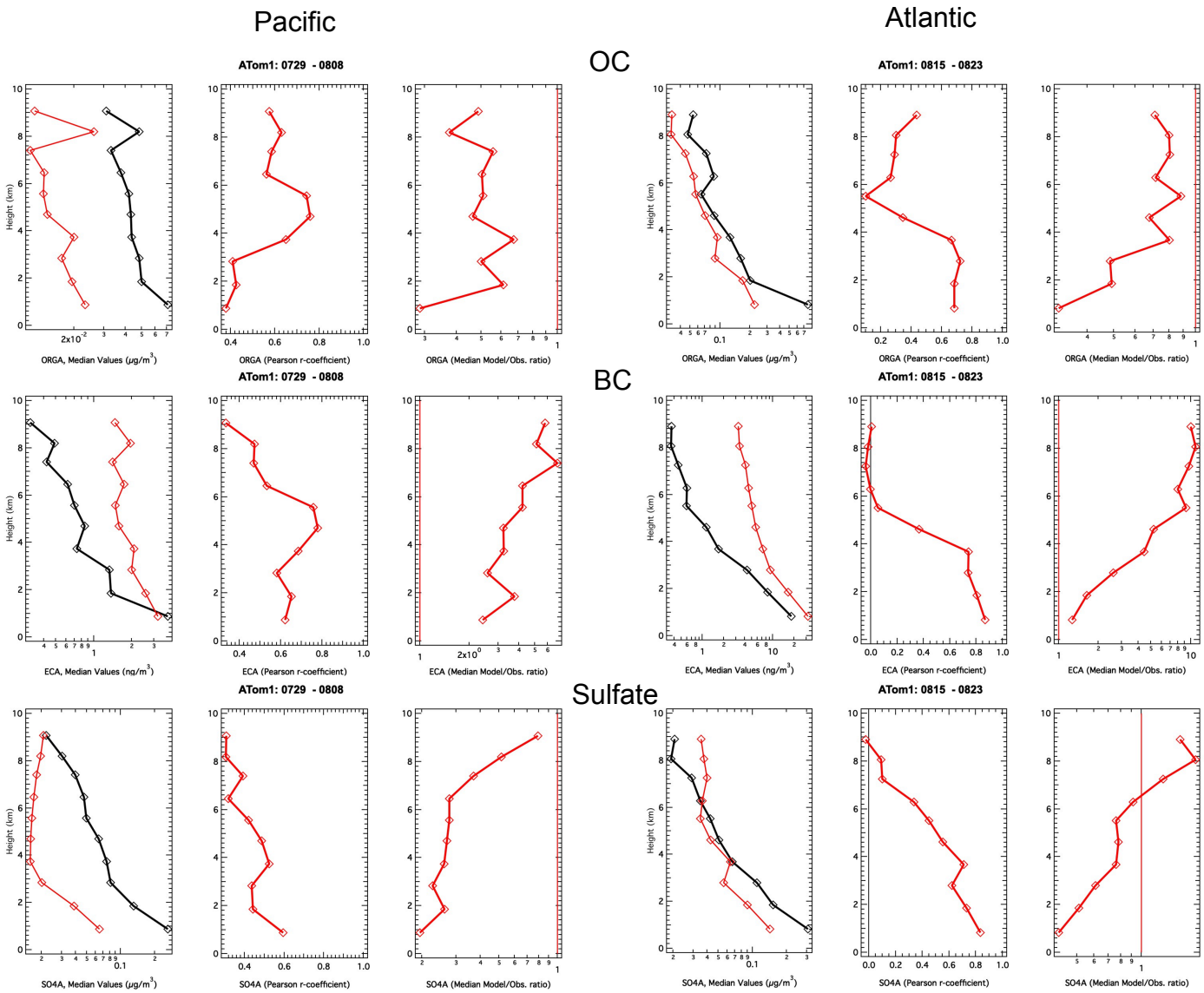

Figure 16. Vertically resolved statistical comparisons of OC, BC and sulfate for the DC-8 flight tracks over the Pacific (July 29-August 8) and Atlantic (August 15-23).

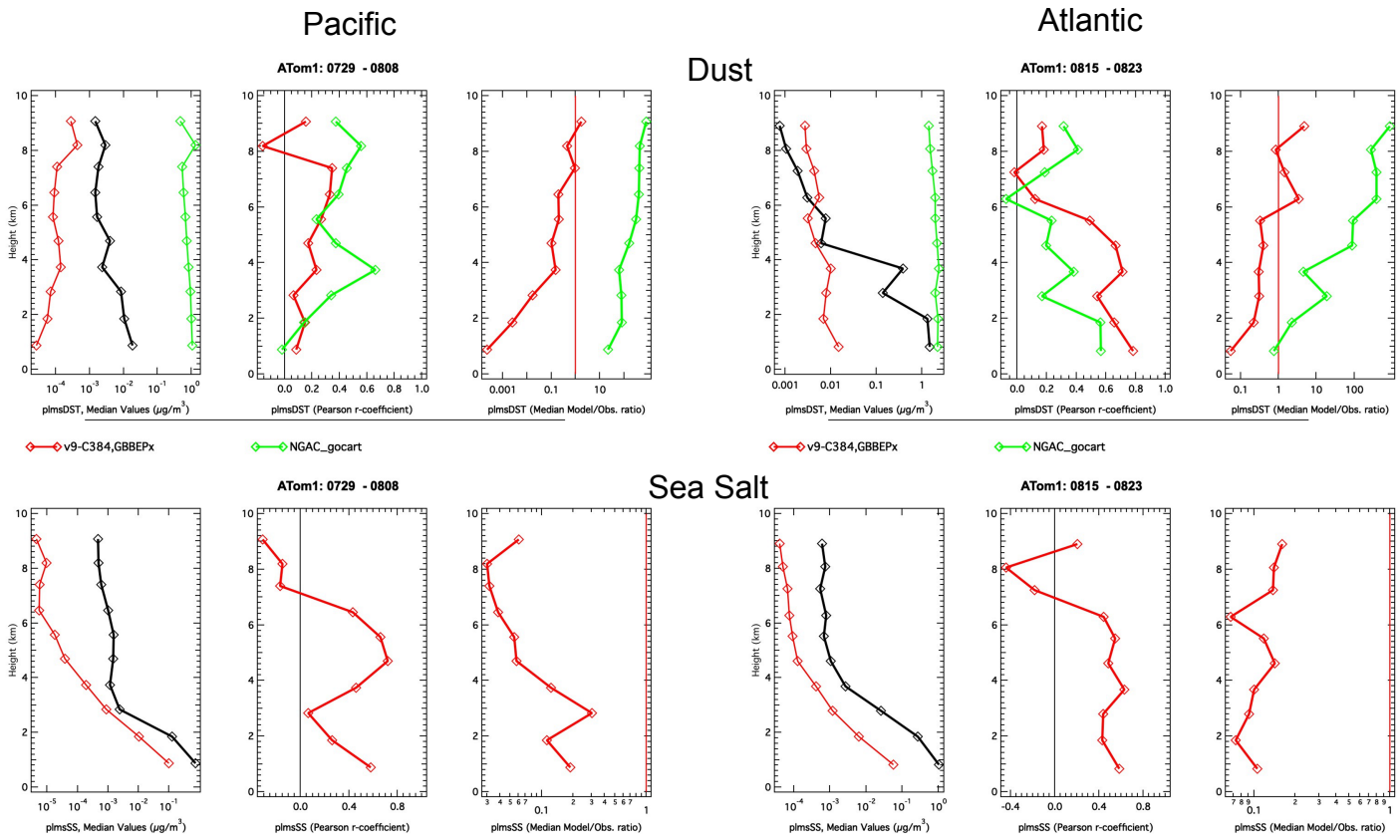

Figure 17. Vertically resolved statistical comparisons of dust and sea salt for the DC-8 flight tracks over the Pacific (July 29-August 8) and Atlantic (August 15-23).

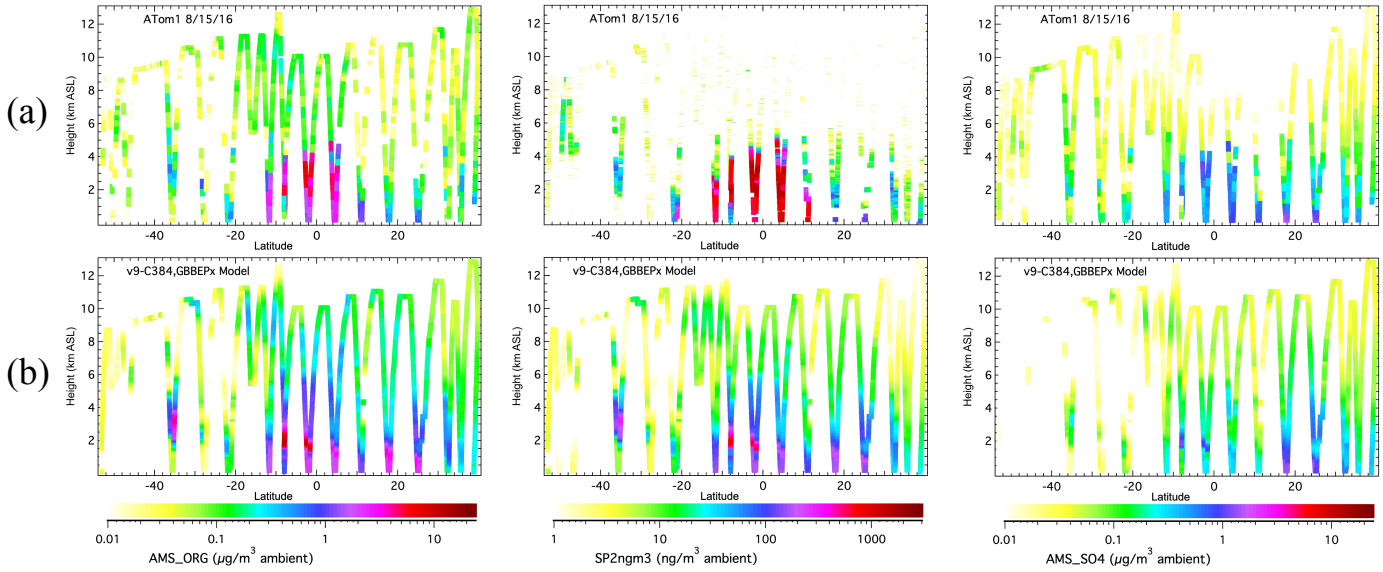

Figure 18. Height-latitude profiles of OC, EC and sulfate over Atlantic on August 15 and 17th, 2016 for (a) the ATom-1 DC-8 observations; (b) GEFS-Aerosols.

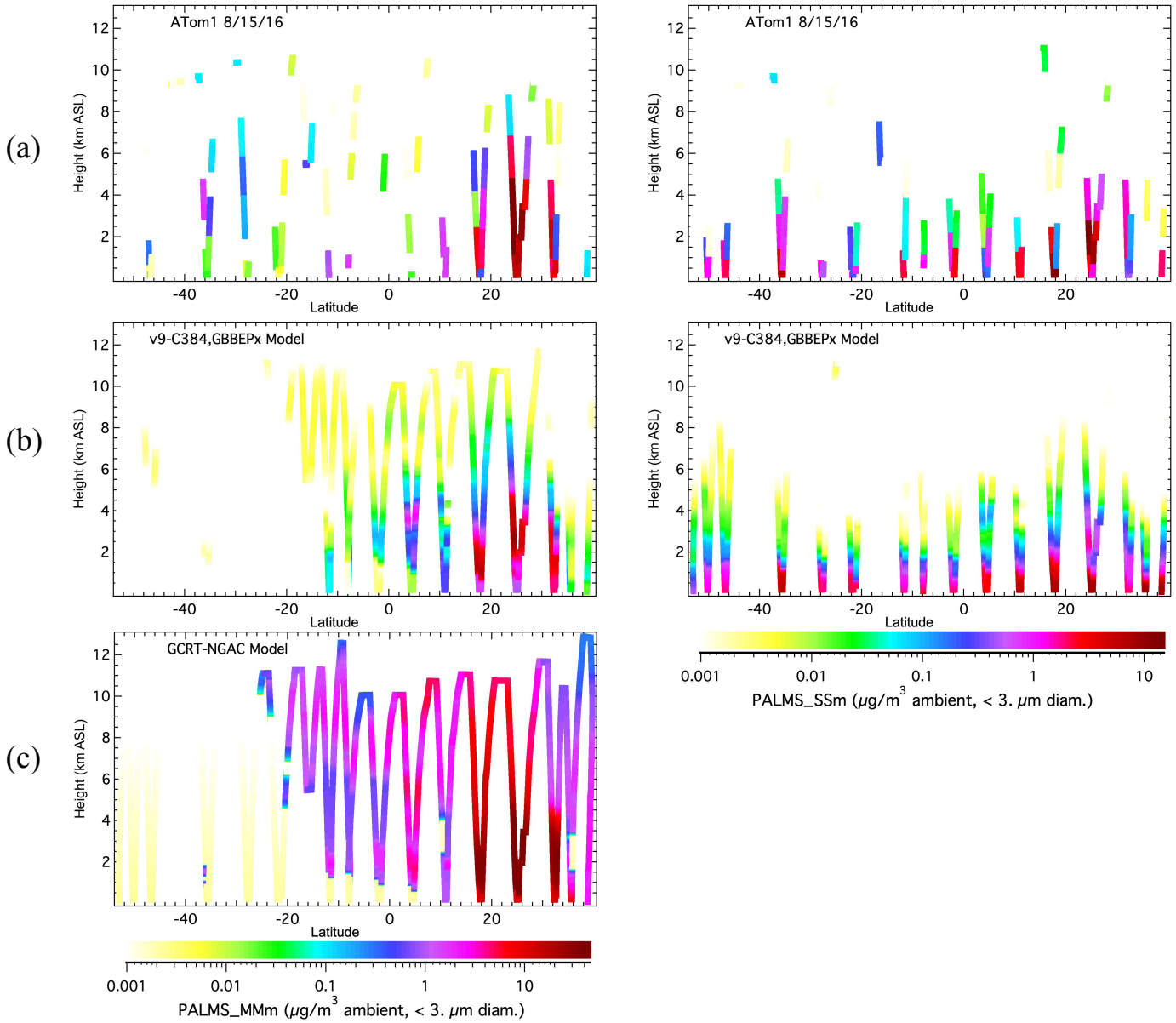

Figure 19. Height-latitude profiles of dust and sea salt over Atlantic on August 15 and 17th, 2016 for (a) the ATom-1 DC-8 observations; (b) GEFS-Aerosols; and (c) NGACv2.